OULU 2019
C 732

ACTA UNIVERSITATIS OULUENSIS

Henna Ruokamo

TIME-GATING TECHNIQUE FOR A SINGLE-PHOTON DETECTION-BASED SOLID-STATE TIME-OF-FLIGHT 3D RANGE IMAGER

UNIVERSITY OF OULU GRADUATE SCHOOL;
UNIVERSITY OF OULU,
FACULTY OF INFORMATION TECHNOLOGY AND ELECTRICAL ENGINEERING;
INFOTECH OULU

ACTA UNIVERSITATIS OULUENSIS
C Technica 732

HENNA RUOKAMO

TIME-GATING TECHNIQUE FOR A SINGLE-PHOTON DETECTION-BASED SOLID-STATE TIME-OF-FLIGHT 3D RANGE IMAGER

Academic dissertation to be presented, with the assent of the Doctoral Training Committee of Information Technology and Electrical Engineering of the University of Oulu, for public defence in the Wetteri auditorium (IT115), Linnanmaa, on 20 December 2019, at 12 noon

UNIVERSITY OF OULU, OULU 2019

Acta Univ. Oul. C 732, 2019

Supervised by
Professor Juha Kostamovaara

Reviewed by
Professor Robert K. Henderson
Professor Angel Rodriguez-Vázquez

Opponent
Professor Ari Paasio

ISBN 978-952-62-2474-9 (Paperback)
ISBN 978-952-62-2475-6 (PDF)

ISSN 0355-3213 (Printed)
ISSN 1796-2226 (Online)

Cover Design
Raimo Ahonen

JUVENES PRINT
TAMPERE 2019

Ruokamo, Henna, Time-gating technique for a single-photon detection-based solid-state time-of-flight 3D range imager.

University of Oulu Graduate School; University of Oulu, Faculty of Information Technology and Electrical Engineering; Infotech Oulu

Acta Univ. Oul. C 732, 2019

University of Oulu, P.O. Box 8000, FI-90014 University of Oulu, Finland

Abstract

Solid-state 3D range imagers have attracted interest in recent years due to their robustness and the possibilities for achieving small and inexpensive realization, which is often required in fields of technology such as robotics, gaming, vehicle safety and hand-held devices, for example. Time-of-flight (TOF) techniques that illuminate the scene with a laser source and detect the backscattered light by means of a single-photon avalanche diode (SPAD) array implemented in complementary metal oxide semiconductor (CMOS) technology have the potential to achieve these requirements with low optical illumination power.

This thesis is concerned with the development of a solid-state 3D range imager based on use of the sliding time-gate technique in a SPAD array and short (~200 ps), intensive laser pulses. The area of the in-pixel electronics needed in time-gated imagers is small, which leads to a high fill factor and a possibility for implementing large arrays. The use of short laser pulses increases the precision and frame rate, since depth measurement can be limited to the range of interest, e.g. around the surface of the target. To increase the frame rate further, the array can be divided into subarrays with independently defined ranges. Tolerance of high background light is achieved by using sub-ns time-gate widths.

A SPAD array of 80 x 25 pixels is developed and realized here. The array is divided into 40 subarrays, the narrow (<0.8 ns) time-gating positions for which can be set independently. The time-gating for each of the subarrays is selected separately with an on-chip DLL block that has 240 outputs and a delay grid of ~100 ps. The fill factor of the sensor area is 32%. A 3D range image measurement at ~10 frames per second with centimetre-level precision is demonstrated for the case of passive targets within a range of ~4 metres and a field of view of 18 × 28 degrees, requiring an average active illumination power of only 0.1 mW. A frame rate of 70 range images per second was achieved with a higher laser average illumination power (~5 mW) and pulsing rate (700 kHz) when limiting the scanning range for each subarray to 30 cm around the surfaces of the targets.

An FPGA-based algorithm which controls the time-gating of the SPAD array and produces the range images in real time was also developed and realized.

Keywords: 3D imager, pulsed TOF imager, range imager, range-gating, SPAD array, time-gating, time-of-flight camera

Ruokamo, Henna, Yksittäisiä fotoneja ilmaisevan vastaanottimen aikaportitustekniikka 3D-laseretäisyysmittaukseen.
Oulun yliopiston tutkijakoulu; Oulun yliopisto, Tieto- ja sähkötekniikan tiedekunta; Infotech Oulu
Acta Univ. Oul. C 732, 2019
Oulun yliopisto, PL 8000, 90014 Oulun yliopisto

Tiivistelmä

Kolmiulotteisten kohteiden etäisyyksien mittaaminen edullisesti toteutettuna pienen sensorin avulla on herättänyt kiinnostusta monilla sovellusalueilla kuten esimerkiksi robotiikassa, autoteollisuudessa ja peliteollisuudessa. Eräs tapa toteuttaa tällainen etäisyysmittalaite on valaista näkymä laserilla ja mitata valosignaalin lentoaika sensorimatriisilla, joka on toteutettu integroituna piirinä CMOS-tekniikalla. Kun sensorit toteutetaan yksittäisiä fotoneja ilmaisevien vyörypurkausdiodien avulla (SPAD), etäisyysmittaus on mahdollista pienellä optisella valaistusteholla ja ilman mekaanisesti liikkuvia osia.

Tässä työssä on tutkittu SPAD-matriisin elektronisen aikaportituksen käyttöä lyhyen (~200 ps) ja intensiivisen laserpulssin kanssa 3D-etäisyysmittauksessa. Etäisyysmittauksen toteutus aikaportituksen avulla antaa hyvän täyttöasteen fotosensoreille, koska tarvittavan elektroniikan määrä pikseliä kohden on pieni. Tällöin myös suurten matriisien toteutus on mahdollista. Lyhyen ja intensiivisen laserpulssin avulla voidaan saavuttaa tarkka ja nopea etäisyysmittaus, kun mittausajanhetki ennakoidaan edellisessä mittauksessa vastaanotetun signaalin perusteella. Nopean kuvataajuuden saavuttamiseksi sensorimatriisi on tässä työssä jaettu alilohkoihin, joita voidaan ohjata mittaamaan kohteita eri etäisyyksillä yhtä aikaa toisistaan riippumatta. Taustavalon vaikutus on minimoitu käyttämällä lyhyttä (<0.8 ns) aikaikkunaa mittauksissa.

Työssä on suunniteltu ja toteutettu integroitu sensoripiiri, jonka ydin on 80 x 25 pikselin SPAD-matriisi. Matriisi on jaettu 40 alilohkoon, joiden toimintaa voidaan ohjata erikseen. Jokaisen alilohkon ohjaussignaalit valitaan integroidulla piirillä olevan viivelukitun viivelinjan 240 lähtösignaalista. Sensorin täyttöaste on 32 %. 3D-etäisyysmittaus ~10 kuvan päivitystaajuudella on demonstroitu passiivisella kohteella ~ 4 m etäisyydellä senttimetriluokan tarkkuudella laserin keskimääräisen optisen valaistustehon ollessa vain 0,1 mW. Suurentamalla laserin keskimääräistä optista tehoa (~ 5 mW) ja pulssitustahtia (700 kHz) voidaan 3D-etäisyyskuvan tahtia nopeuttaa esimerkiksi 70 kuvaan sekunnissa, kun jokaisen alilohkon mittaussyvyys rajoitetaan 30 cm kohteen ympärille.

Työssä kehitettiin myös algoritmi, jolla voidaan ohjata SPAD-matriisia ja tuottaa etäisyyskuvia reaaliajassa.

Asiasanat: 3D-etäisyysmittaus, aikaportitus, pulssin kulkuaikamittaus, SPAD-matriisi, syvyyskamera, TOF-kamera

Acknowledgements

First, I would like to thank Professor Juha Kostamovaara who supervised this PhD research. I am very grateful for all the advice and encouragement he has given me during these years. Our conversations have always been a pleasure thanks to his great sense of humour. Thanks also go to Harri Rapakko and Lauri Hallman for all the help they have given during this research and as co-authors of the papers, and similarly to Matti Polojärvi for bonding the ICs and ordering the components. I would also like to thank my roommate Sahba Jahromi for discussions about SPAD sensors and for sharing the frustrations of writing a thesis. I am sure her thesis will be amazing. I am also very grateful to my other colleagues in the Circuits and Systems research group for entertaining conversations during coffee breaks and lunch times.

I acknowledge funding received for this research from the Infotech Oulu Graduate School and the Academy of Finland, and likewise grants from the Finnish Foundation for Technology Promotion (Tekniikanedistämissäätiö. TES), the Seppo Säynäjäkangas Foundation, the Tauno Tönning Foundation and the Information Technology and Electronics Society (Tietotekniikan ja elektroniikan seura, TiES).

I would like to thank the reviewers of this thesis, Professor Robert Henderson of the School of Engineering at the University of Edinburgh and Professor Angel Rodríguez-Vázquez of the Seville Institute of Microelectronics and the University of Seville, for their very valuable feedback on the thesis. I am also grateful to Malcolm Hicks for checking the English language of the thesis, and for not only correcting the spelling but also suggesting better ways of formulating the more complicated sentences.

I would like to thank my friends and family for their encouragement during my doctoral studies and all the other activities that made it possible for me to lead a full life. And most especially I wish to thank my husband Tuukka and our sons Onni and Topias for supporting and encouraging me during these years.

Oulu, October 2019 Henna Ruokamo

Abbreviations and definitions

3D	three-dimensional
ADC	analogue-to-digital converter
APD	avalanche photodiode
BSI	back-side illumination
cw-iTOF	continuous wave indirect time-of-flight
CAPD	current-assisted photonic demodulation
CCD	charge-coupled device
CIS	complementary metal oxide semiconductor image sensor
CMOS	complementary metal oxide semiconductor
CW	continuous-wave
cps	counts per second
DCR	dark count rate
DLL	delay-locked loop
DNL	differential nonlinearity
E	energy
e.g.	exempli gratia
etc.	et cetera
FF	fill factor
FLIM	fluorescence-lifetime imaging microscopy
FOV	field of view
FPGA	field-programmable gate array
fps	frames per second
FR	frame rate
FWHM	full width at half maximum
HV	high voltage
i.e.	id est
iTOF	indirect time-of-flight
IC	integrated circuit
INL	integral nonlinearity
LiDAR	Light detector and ranging
mmWave	millimetre wave
MUX	multiplexer
NIR	near-infrared
pl-iTOF	pulsed indirect time-of-flight
PDP	photon detection probability

PMD	photon mixing device
PMT	photomultiplier tube
PSR	partial scanning range
SIPO	serial-in parallel-out
SPAD	single photon avalanche diode
STI	shallow trench isolation
TCSPC	time-correlated single photon counter
TDC	time-to-digital converter
TOF	time-of-flight
USB	universal serial bus

φ	phase difference
σ	standard deviation
λ	wavelength

c	speed of light
d	distance
D_{amb}	ambiguity range
f	frequency
f_{pulse}	laser pulsing rate
I_{SPAD}	current
t_{TOF}	time-of-flight of a source signal
V_{BD}	breakdown voltage
VDD	positive supply voltage
V_{EX}	excess bias voltage

Original publications

This thesis is based on the following publications, which are referred throughout the text by their Roman numerals:

I Ruokamo, H., Rapakko, H., & Kostamovaara, J. (2017). An 80 × 25 pixel CMOS single-photon image sensor with sub-ns time gating for solid-state 3D scanning. *13th Conference on Ph.D. Research in Microelectronics and Electronics (PRIME)*, 365-368.

II Ruokamo, H., Hallman, L., Rapakko, H., & Kostamovaara, J. (2017) An 80 × 25 pixel CMOS single-photon range image sensor with a flexible on-chip time gating topology for solid state 3D scanning. *ESSCIRC 2017 - 43rd IEEE European Solid State Circuits Conference,* 59-62.

III Ruokamo, H., Hallman, L. W., & Kostamovaara, J. (2019). An 80 × 25 pixel CMOS single-photon sensor with flexible on-chip time gating of 40 subarrays for solid-state 3-D range imaging. *IEEE Journal of Solid-State Circuits, 54*(2), 501-510.

IV Ruokamo, H., Hallman, L., & Kostamovaara, J. (2019). A range-gated CMOS SPAD array for real-time 3D range imaging, *IS&T Electronic Imaging: Image Sensors and Imaging Systems Proceedings,* 357-1-357-5.

The author with the help of co-authors wrote Papers I- IV. The author of this thesis designed the integrated circuit (IC) which was used as an image sensor in Papers I - IV and also the measurement environment including the printed circuit board on which the IC was bonded, digital design implemented on FPGA for controlling the IC and software that was used in the measurements. The author of this thesis also conducted the measurements for Papers I-IV. The system was designed in co-operation with Harri Rapakko for Papers I-II and the laser pulsing circuitry was designed in co-operation with Dr. Lauri Hallman. The work was supervised throughout by Prof. Juha Kostamovaara. In this thesis, some previously unpublished results are also presented.

Contents

1 Introduction

1.1 Background

A 3D range image is a 2D map showing distances from points on the target surface measured within the field-of-view of the imager. Thus, contrary to a conventional camera, which measures only the intensity of the radiant excitation of points within a 2D object surface, a 3D imager can determine the distance of each point on the surface with a certain spatial resolution, see illustration in Fig. 1. A 3D range imager is typically realized with a laser scanner that measures distances from objects on one or more horizontal planes, while the measurement beam (or several beams on different horizontal planes) will rotate around the measurement scene. Laser scanners of this kind have traditionally been used in geodesy, civil engineering, architecture, inspection, quality control and quality assurance, for example. The development of an autonomous or "driverless" car is an example of an application that obviously calls for high-speed environment-sensing techniques (Hecht, 2018). There is, however, a growing interest in applying 3D range imaging techniques in areas beyond the traditional ones mentioned above, e.g. in robotics and automation, security, 'smart homes', gesture control and collision avoidance systems for unmanned aerial vehicles.

Fig. 1. A range image shows distances to points on the surface of an object.

These fields of application can be roughly categorized into long-range (100 m – 1 km), mid-range (10 m – 100 m) and near-range (1 m – 10 m) applications. Although the precision and measurement range required will depend greatly on the application, a frame rate of 10 frames/s or higher is preferred in most cases. A measurement precision of ~10 cm is often acceptable in long-range applications, but in some near-range cases such as face recognition mm-level precision is required. In addition, especially in new, emerging applications, a solid-state

approach to scanning, i.e. an architecture requiring no mechanically moving parts, is preferred. Such a realization would simplify the system and pave the way for miniaturization, low power consumption, low costs and high reliability.

For ranges greater than >10 m, laser detection and ranging devices (LiDARs) are typically used to measure the distance to the target along a single optical axis. As pointed out above, when 2D or 3D range image information is needed the scene is typically scanned using a spinning measuring head or rotating mirrors which direct the laser beam within the system's field-of-view (FOV). The problem with these techniques is their non-solid-state implementation, which results in high costs, high power consumption and relatively large size. Microwave radar techniques are also used for measuring distances in long-range applications, as they offer good visibility through smog and rain, although even with the new mmWave techniques that provide better distance resolution than traditional radars, the spatial resolution (transversal resolution) is still usually poor compared with laser-based optical radar systems (Mukhtar, Xia, & Tang, 2015; Peng, Chen, Kao, Chen, & Lee, 2015).

For ranges shorter than a few metres there are also other techniques available for achieving distance measurements with high spatial resolution, e.g. structured light and stereovision-based solutions. A popular choice nowadays in consumer products intended for ranges of up to ~5 m is the time-of-flight technique, which uses in-pixel demodulation techniques to distinguish the phase difference between the transmitted modulated light and the received echo signal (Kato et al., 2018; Kraft et al., 2004; Payne et al., 2014). The pixel count of a sensor of this type is already high (up to 1 Mpixel) and good precision (~1 cm) can be achieved, but this technique requires relatively high illumination power (typically ~100 mW or more) and has limited tolerance of high levels of ambient light.

One obvious option for achieving a higher frame rate or a longer measurement range is to increase the optical power in the transmitter. There are limits to the optical laser power, however, due to eye safety issues, especially at visible and NIR (near infrared) wavelengths. Lasers operating at wavelengths of 800 – 950 nm are usually good options, since they give good performance and the sensors can be realized in standard Si-based CMOS technologies. Also, longer wavelengths (e.g. 1550 nm) are especially useful in automotive LiDARs to achieve higher ranges, since a higher eye-safe optical power can be used, but then a special (and expensive) processing technique is needed for the sensor, e.g. that employing InGaAs/InP.

Another solution for improving the performance of a range imager system is to use higher sensitivity in the optical detector. From this point of view, single photon avalanche diode (SPAD) detectors which are able to detect a low power

echo signal even at the single photon level have become an interesting option due to their good timing resolution and the possibility for implementing them in a standard CMOS technology. Pulsed laser rangefinders that measure the time-of-flight of optical pulses with a SPAD array and time-to-digital converters (TDC) have achieved good performance even with only a single photon detected from the laser pulse echo (Jahromi, Jansson, & Kostamovaara, 2016; Shin et al., 2016). A solid-state 3D range imaging system of this type is presented in Fig. 2. The system uses a pulsed laser source, the energy from which is sent through a diffuser into the field-of-view (FOV) of the range image sensor so that the distance can be calculated from the measured time-of-flight (t_{TOF}) of the detected photons based on the known speed of light (c = 299 792 458 m/s). The FOV of the system is set by means of suitable optics depending on the targeting application.

The drawback of single photon detection techniques is that the sensor is also highly sensitive to photons arriving from any ambient light source. For this reason single photon sensors have typically shown high performance only in dark or dim lighting conditions. An optical filter is usually placed in front of the receiver, but, other additional noise reduction techniques such as spatial and temporal correlation of the photons have been proposed for detecting low optical power echo signals even in high ambient lighting conditions (Henderson, Johnston, Hutchings et al., 2019; Niclass, Soga, Matsubara, Kato, & Kagami, 2013). One solution for obtaining a single photon sensor to cope with high ambient lighting conditions is to use time gating, which activates the SPAD sensor for only short periods of time, just when needed (Kostamovaara et al., 2015). When the sensor is activated for only a short period of time photons from the ambient light source that reach the sensor outside this active period have no effect on its operation.

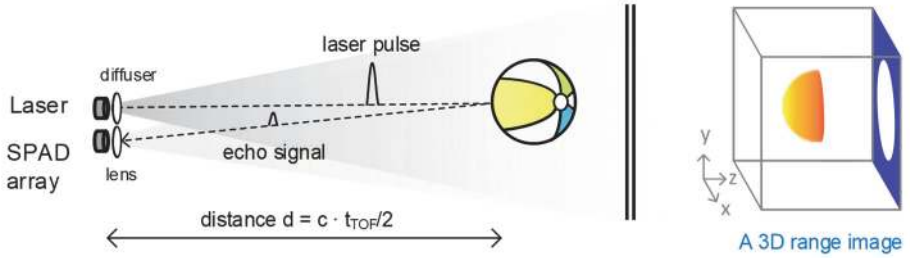

Fig. 2. Solid-state 3-D range imaging with a pulsed laser source using the time-of-flight technique.

Time gating has also been used in range-gated cameras, which use an active laser source and a gated camera to produce a 2D range map (Andersson, 2006; Busck & Heiselberg, 2004). An image intensifier is usually used in a range-gated camera system to increase the sensitivity of the CCD sensor and enable fast electronic gating. This provides high accuracy at a high frame rate, but also entails a high cost. High accuracy have been demonstrated recently also with range-gated quanta image sensor (Ren et al., 2018).

1.2 Objectives and scope

The main goal of this work is to develop a 3D range imager architecture and a CMOS realization of it which is based on the use of a short, energetic laser pulse (FWHM~100-200 ps, E>1 nJ, λ~860 nm) in the transmitter and a time-gated SPAD array receiver to produce 3D range images of scenes under illumination. Contrary to the standard gating approach, however, the time-gating of the SPAD array is used in this work not only to limit the effect of ambient lighting but also to produce the 3D range image data as such. Each SPAD in the pixel array is activated once for each laser pulse and the length of the time gate for measuring the signal is minimized (<1 ns) in order to achieve maximal suppression of the effect of the background illumination and to produce the 3D range image information on the basis of the position of the time gate alone. By shifting the time gate in smaller steps than the actual time gate (i.e. employing the sliding time-gate technique) better timing resolution can be achieved. In conclusion, by using a short time-gate the effect of noise can be decreased but the timing information can still be achieved without the need for a separate TDC operation for each SPAD.

Time-gated SPAD array chips are usually relatively simple relative to time-to-digital converter (TDC)-based solutions and have achieved the highest pixel counts of all SPAD arrays to date, 512 x 512 (Ulku et al., 2019), but they are usually implemented for other applications than 3D range imaging, e.g. for fluorescence-lifetime imaging microscopy (FLIM) applications with correspondingly different system and chip level requirements.

The objective of this work was to develop a solid-state 3D range imager that is capable of measuring distances of up to few metres with ~cm resolution in normal office lighting (and preferably even brighter) conditions (at the illumination power level indicated above). The frame rate of the system should be high enough to be able to measure the movement of a human being in real time. The targeting application could be a gesture controlling system, for example.

1.3 Structure of the thesis

This work, which is a summary of the original Papers I-IV, describes the development and testing of a solid-state 3D range imager that illuminates the scene with short laser pulses and detects the photon echoes from that pulse with a time-gated SPAD array.

The brief review of optical solid-state 3D range imager techniques in chapter 2 concentrates principally on single photon detector-based indirect and direct time-of-flight measurements, together with other typical solid-state optical 3D imaging techniques.

The time-of-flight technique using time gating of a SPAD array and short laser pulse illumination is presented in chapter 3. When a depth image is produced using a short, sub-ns laser pulse and scanning the scene with a sliding time-gate technique, the frame rate of the resulting 3D range image may be lowered if high depth resolution and a long range are needed. To increase the speed of the depth measurement in order to be able to measure fast movements of the target, the sensor array (and thus also the system FOV) is divided here into subarrays, the scanning range and scanning depth of which can be independently controlled. An example of the controlling algorithm for subarrays based on a field-programmable gate array (FPGA) is also described.

The electronic design of the SPAD array chip is described in more detail in chapter 4, and chapter 5 shows several examples of 3D range imaging results obtained with different setups. In particular, it demonstrates the system's tolerance with respect to background lighting and presents results regarding the maximum frame rate. Chapter 6 contains a discussion of the work and also some recommendations for possible future developments. A summary of the thesis is given in chapter 7.

2 Solid-state optical 3D imaging techniques

There are several non-optical 3D imaging techniques that use the microwave range of the electro-magnetic spectrum (e.g. differential GPS, microwave radar and SAR interferometry), but these are not suitable for range measurements with high angular resolution because of the limitation on diffraction. At optical wavelengths the diffraction limit (θ_{min} ~λ/D) is much less severe, and thus higher spatial resolution is available. Most of the solid-state optical 3D imagers that are able to measure distances of up to a few metres use either triangulation or various time-of-flight (TOF) techniques. A brief overview of the most commonly used optical range imaging techniques is given in Fig. 3.

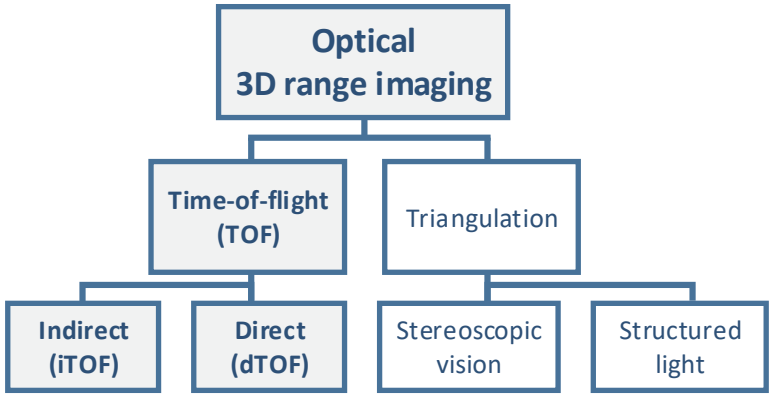

Fig. 3. Solid-state optical 3D imaging techniques

One well-known conventional optical distance measurement technique uses the triangulation principle. Triangulation-based approaches can be divided into passive and active imaging systems, the operating principles of which are described briefly in chapter 2.1. Chapter 2.2 presents a time-of-flight technique in which a continuous wave (CW) modulated laser transmitter is used and the per-pixel distance from the target is determined from the phase of the received signal using an active CMOS pixel sensor, while chapter 2.3 focuses on the topic of this thesis, which is single photon detection-based 3D range imaging. In particular, the structure and operating principle of a CMOS single photon detector (SPAD) is explained. At the system level, indirect and direct single photon detection-based TOF 3D range imager techniques are discussed and compared.

2.1 Triangulation-based approaches

Triangulation-based approaches can be divided into passive and active imaging systems. Passive imaging systems are based on background illumination only and do not actively send out any energy for imaging purposes. Passive triangulation is perhaps the oldest distance measurement technique, having evolved from the early tape-based measuring technique to yield camera-based stereovision systems.

Active imaging systems send energy into the surroundings, i.e. they use optical illumination. Active triangulation techniques include structured light techniques, which are widely used in consumer products to measure the ranges of points in a scene. The principles of both passive and active triangulation are presented briefly below.

2.1.1 Passive triangulation

Perhaps the oldest distance measurement technique of all is that based on passive triangulation. This is a geometrical method in which one point on the surface of the object and two points in the measurement system are used to construct a geometrical triangle. When the distances of two points in the measurement system are known and the angles with the target have been measured, the distance to the object can be calculated, see example in Fig. 4 (a). The passive triangulation technique can be implemented with two cameras that are placed at a known distance away from each other, for example. This type of system uses stereovision much like human eyes. To solve it one needs the distance between the cameras (baseline) and a high computation processing power to produce the distance information. Camera-based systems without active illumination need high-contrast scenes and consequently experience problems in the dark, for example.

2.1.2 Active triangulation

Active triangulation techniques use active illumination of the scene with a specially designed light pattern, so that distances can be calculated from the deformation of the light pattern in the captured image, see Fig. 4 (b) (Van der Jeught & Dirckx, 2016). The active light can be points, lines or special patterns generated by projecting incoherent light or laser beams onto the field of view of the receiver. Structured light-based 3D range imagers have been implemented in commercial products, e.g. Microsoft Kinect V1, Intel RealSense R200 and Apple iPhone X. The

active illumination solves the problem of the high-contrast scenes needed in passive triangulation and will thus also work in dark. The drawback with this technique is the same as in passive triangulation, however, that a large baseline is needed to achieve high resolution for depth measurement over distances longer than a few metres. Also, the illumination power limits the measurement range when the projector needs to be miniaturized for use in handheld devices, for example (Geng, 2011; Van der Jeught & Dirckx, 2016).

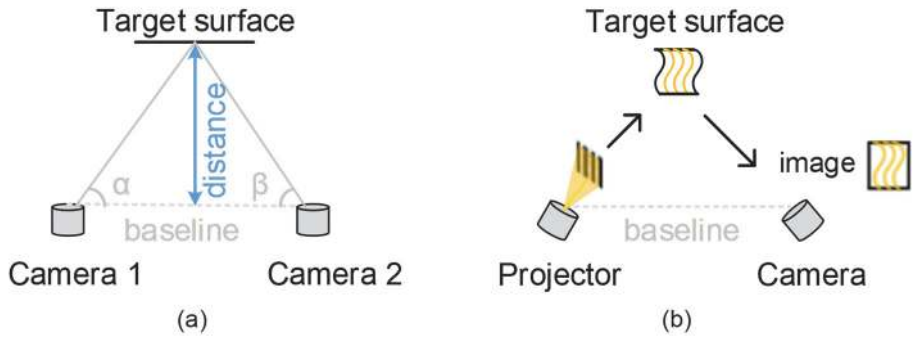

Fig. 4. (a) The passive triangulation principle. (b) The triangulation-based technique with active structured light illumination.

2.2 Time-of-flight technique with in-pixel photo-mixing devices

The problem of the baseline needed in triangulation can be solved by measuring distances with time-of-flight techniques, in which the time-of-flight (t_{TOF}) of a source signal travelling to the target and back to the receiver is measured. The distance d can then be calculated from this information, since the speed of the signal (c = the speed of light) is known, hence $d = c \cdot t_{TOF}/2$.

A popular technique for measuring time-of-flight is to measure the phase shift between the transmitted and received continuous-wave echo signals. This indirect technique is often used with in-pixel photon-mixing device sensors (Pancheri & Stoppa, 2013), see the operation principle in Fig. 5. The phase difference (φ) is typically determined by integrating the received signal in four phases (Q_1 -Q_4), each of which has a 90-degree phase difference, as is shown in Fig. 5. Since the method is based on phase measurement, the maximum measurement range is limited by the ambiguity range D_{amb}. This drawback can be solved by using a lower modulation frequency, which will increase the range, albeit at the cost of lower precision. Another option is to use multiple frequencies to solve the aliasing problem and

thereby achieve longer ranges without sacrificing accuracy. This latter approach is implemented in most advanced continuous-wave TOF imagers (Bamji et al., 2018).

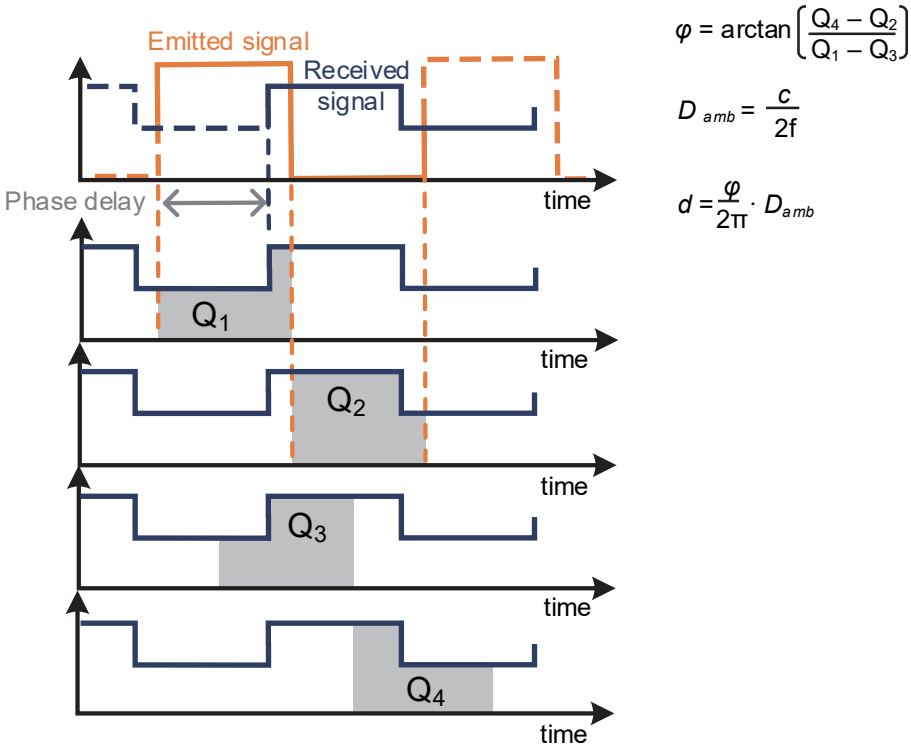

Fig. 5. A time-of-flight measurement technique in which the distance is determined from the phase difference between the emitted and received signals by sampling the received signal in four phases Q_1-Q_4.

In-pixel photo-mixing devices realize light detection and the demodulation of high frequency signals directly in the pixel. The first such devices were produced with photogate-pixels which used gate voltage modulation in CCD technology (Miyagawa & Kanade, 1997; Schwarte et al., 1997; Spirig, Seitz, Vietze, & Heitger, 1995), while the first successful realization of an all-solid-state 3D TOF range camera that was based on a dedicated sensor involved the continuous-wave modulation of light detected with customized CCD/CMOS pixels (Lange & Seitz, 2001). Later pixels in standard CMOS and CIS technologies were proposed in order to reduce the cost of the imager.

In-pixel photo demodulators have become the most popular type of 3D imaging sensor commercially available at the moment. These include the photogate demodulation pixels implemented in Microsoft Kinect devices (Bamji et al., 2018; Payne et al., 2014) and the photon-mixing devices (PMD) (Schwarte et al., 1997) used in pmd technology products. Current-assisted photonic demodulation (CAPD) pixel-based sensors (Kato et al., 2018; Van der Tempel, Grootjans, Van Nieuwenhove, & Kuijk, 2008) are used nowadays in Sony DepthSense solutions, for example. Although they already provide high pixel counts (up to 1M pixels), improvements in range (usually max ~6 m), power consumption and sensitivity (high optical power) are needed. In addition, these sensors saturate in high ambient light conditions and are thus unable to measure the depth image of the scene unless background light cancellation techniques are used (Hsu, Liao, Lee, & Hsieh, 2018).

2.3 Time-of-flight imagers based on single photon detection

Single photon avalanche diode-based time-of-flight imaging systems have attracted interest in recent years due to their high sensitivity, good timing resolution and fairly simple post-processing needs. The single photon level of sensitivity can be exploited to reduce the optical power needed, and the low timing jitter is related to good range measurement precision. The basic operating principles and structures of typical single photon detectors and how they are arranged to form the 2D array needed for solid-state imaging applications are presented in section 2.3.1. The time-of-flight can be measured by the continuous-wave phase comparison technique applied to an array of demodulator pixels, as described in the previous section, or alternatively with an array of single photon detectors. The use of this indirect time-of-flight technique with a SPAD array is described in section 2.3.2 and that of the direct time-of-flight technique with a SPAD array in section 2.3.3.

2.3.1 Single photon detectors

The most sensitive light detectors are single photon detectors, since they are able in principle to detect a signal even from a single photon. The first single photon detectors were photomultiplier tubes (PMT), as first proposed (Morton, 1949). These are large sensors, however, needing a high operating voltage (>1000 V) and having a limited number of pixels, which makes them unsuitable for imaging applications (Privitera et al., 2008).

Single photon avalanche diodes (SPADs) have gained in popularity recently since they can be integrated into standard CMOS technology, which not only enables the inclusion of electronics in the sensor chip but also makes the sensor inexpensive when mass-produced. Typical structures and performance parameters of a SPAD are described in the next section, followed by a discussion of the kind of electronics that is usually implemented on-chip in SPAD sensors and the issues that have to be considered when SPADs are arranged in large arrays.

Single-photon avalanche diodes (SPADs)

A SPAD is a photodiode reverse-biased above the breakdown voltage, a region in which even one photon can trigger a large avalanche current through the diode. This large current is then sensed and usually transferred to a digital signal, which indicates that a SPAD has been triggered. After triggering, the SPAD is quenched and then reverse-biased above the breakdown voltage again so as to be ready to detect a new photon. Both SPADs and avalanche photodiodes (APD) use the avalanche current of a semiconductor p-n junction when reverse-biased but an APD functions in the linear region while a SPAD is designed to operate well above the breakdown voltage. A SPAD is sometimes called a Geiger-mode avalanche photodiode.

A typical SPAD realized in standard high voltage (HV) 0.35 µm CMOS technology is a diode formed between p+ and an nwell junction, see Fig. 6 (Rochas et al., 2003). The advantage of this structure is its relatively low noise, its isolation from the substrate and the possibility for implementing readout electronics at low voltage directly from the anode node. In the structure in Fig. 6, a pwell is used to prevent premature edge breakdown, which may cause charge multiplication events triggered by thermal generation if not properly designed. To prevent premature edge breakdown, the electric field has been reduced at the edges of the junction with a diffused guard ring.

Better sensitivity at near-infrared (NIR) wavelengths can be obtained by using a deeper junction for the avalanche region, e.g. between a pwell and a deep nwell (Burri et al., 2014; Pancheri, Stoppa, & Dalla Betta, 2014; Richardson, Webster, Grant, & Henderson, 2011). These structures often have increased timing jitter, however (L. Pancheri, D. Stoppa & G. Dalla Betta, 2014). Increased NIR sensitivity can also be achieved by using the substrate as the anode node, but the lack of substrate isolation between the SPADs and the electronics and the required

capacitive coupling of the readout and quenching circuitry mean that this is not straightforward to implement (M. Perenzoni, Pancheri, & Stoppa, 2016).

In standard deep submicron technologies the noise of the SPAD structure in Fig. 6 increases due to the higher doping levels of the well implantations, but the introduction of deep submicron technologies that have STI and the triple well options that are now available have made new SPAD structures possible. One successful implementation of a large array of SPADs with low noise level has been demonstrated with a p-i-n structure in which the active junction is between the pwell, p-epi and buried nwell (Ulku et al., 2019; Veerappan & Charbon, 2016).

One solution for preventing premature edge breakdown is to reduce the electric field at the edges of the junction (as in Fig. 6), and another possibility is to lower the breakdown voltage for the centre part of the diode. This can be done by means of a special enhancement implant, but although the results are promising in terms of shrinking the area needed for the guard ring, this technique is not available in standard CMOS technologies. Premature edge breakdown is most often prevented by the use of diffused guard rings, as in Fig. 6, but as the technologies evolve and pixel sizes are scaled down other types of guard ring have to be implemented, e.g. “p-epi” guard rings (Pellegrini et al., 2017; Richardson et al., 2011; Ulku et al., 2019).

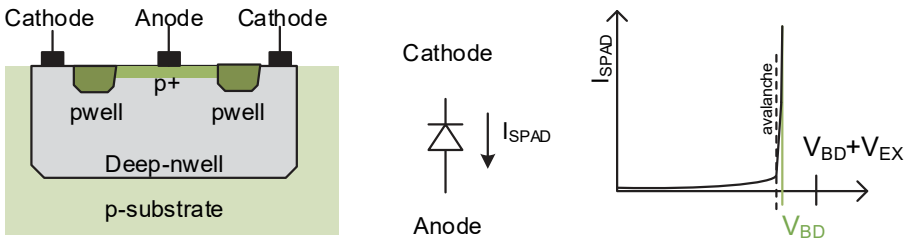

Fig. 6. Typical structure and current-voltage characteristic of a CMOS SPAD.

The intrinsic noise of a SPAD is measured in the form of a dark count rate (DCR), which shows the rate of random triggerings of the SPAD in the dark. The DCR depends on the technology used, the structure of the SPAD, the active area and perimeter of the diode and the excess bias voltage. A larger SPAD and higher excess bias voltage (V_{EX}) will increase the DCR (Richardson et al., 2011).

While higher V_{EX} increases the DCR, it also increases the photon detection probability (PDP), which is the probability of a single photon being detected by a

given SPAD. The PDP of a SPAD depends on the SPAD structure and technology, and is also dependent on the wavelength. SPADs implemented in standard CMOS technology usually have their highest PDP in the visible wavelength spectrum and ~30% PDP levels have been reported for wavelengths of 400-500 nm, which then decrease in the near infrared region to ~5% at 800 nm (Pancheri et al., 2014; Richardson et al., 2011; Stoppa, Mosconi, Pancheri, & Gonzo, 2009).

The timing jitter of a SPAD is an important parameter in timing applications and FWHMs of 50-100 ps have typically been reported for the timing jitter of such a structure, as in Fig. 6. The jitter depends on the depth of absorption of the incident photon and the statistical build-up of the avalanche current, and also on the carrier transit time generated from the depletion layer to the multiplication region (Ghioni et al., 1988). As this is affected by the strength of the electric field, jitter can be reduced by increasing the excess bias voltage. Lateral avalanche propagation may also increase the timing uncertainty in SPADs of larger area.

The dead-time of a SPAD refers to the time period after the triggering of the SPAD until it is ready to detect a new photon. The dead-time is usually set according to the afterpulsing probability of the SPAD. This afterpulsing is caused by fabrication defects, which introduce traps in the forbidden energy band that may be filled during the avalanche event and released again, causing new avalanche events. The afterpulsing probability depends on the intensity of the avalanche current flowing across the junction and decreases when the current decreases or if the time interval before next activation of the SPAD is increased. The dead-time is an important factor in systems where the performance depends on the sampling rate of the SPAD, e.g. in quanta image sensors. The afterpulsing probability nevertheless usually becomes negligible (<1%) when the delay in re-activating an Si SPAD after an avalanche is longer than a few tens of nanoseconds, but sometimes a dead time of 100 ns (Richardson et al., 2011) or even 1µs is needed (Pellegrini et al., 2017; Tisa, Guerrieri, & Zappa, 2008).

The standard CMOS processes are not optimized for the SPAD performance, and the doping levels used in CMOS well implantations increase as the technology node shrinks in order to maintain the performance of the transistors. Increased doping levels increase the DCR of the SPAD, and thus SPAD-based sensors are usually produced in rather conservative technology nodes. The development of SPAD structures is still progressing towards newer technologies, since the higher gate density of digital realizations enables more circuitry to be implemented on-chip, e.g. in the form of in-pixel TDCs with a reasonable fill factor. The number of pixels that is needed in imaging applications is also increasing, and smaller pixel

pitch with higher photon detection efficiency would be desirable (Abbas et al., 2016; Bruschini, Homulle, Antolovic, Burri, & Charbon, 2019). In view of the increased interest in high performance single photon detectors, the development of deep submicron SPAD structures in both standard and custom processes continues.

Pixel electronics

The pixel electronics usually include at least quenching circuitry and circuitry for converting the triggering of the SPAD into a digital output signal. The quenching circuitry quenches the avalanche current after the SPAD has been triggered, which can be done either passively with a resistance or actively using circuitry. Similarly, the time-to-digital converters or photon counters, or both, can be implemented in the pixel, depending on the targeting application. Photon counters are implemented when the photon detection rate is to be measured, e.g. in quanta image sensors, while time-to-digital converters are used for direct TOF measurements, as discussed in more detail in section 2.3.3.

To achieve the minimum number of in-pixel transistors it has been proposed that analogue signal processing (analogue photon counters or time-to-analogue converters) should be used (Dutton et al., 2015; Pancheri, Massari, & Stoppa, 2013; Stoppa et al., 2009). This will enable the number of in-pixel transistors to be minimized and fill factors of >20% to be achieved even in the conservative 0.35 µm technology (M. Perenzoni et al., 2016). The area needed for the digital logic can nevertheless be dramatically reduced by scaling down the gate size of the technology, so that the gate densities of around 25 kgates/mm^2 commonly achieved in 0.35 µm technologies can be increased to around 2 000 kgates/mm^2 in 40 nm technologies, for example. The focus in this thesis will be on digital pixel electronics due to its easy portability into high gate density processes.

SPAD arrays

Time-of-flight detection in solid-state imaging applications is realized over a 2D pixel array, e.g. an array of SPADs. The first SPAD array integrated into standard CMOS technology was proposed in 2003 (Rochas et al., 2003) and an array of 32 × 32 pixels was used for an imaging application in 2005 (Niclass, Rochas, Besse, & Charbon, 2005). Since then, multiple pixel architectures and structures have been proposed for increasing the number of pixels, the fill factor of the sensor and the timing performance of a large SPAD array. The largest SPAD array reported at the

time of writing this thesis, consisting of 512 × 512 SPADs, has been designed for FLIM applications (Ulku et al., 2019), but the fill factor of that large p-i-n SPAD array was only ~10%. SPAD arrays designed for depth imaging applications are usually smaller, especially when a large amount of electronics must be implemented in-pixel. Examples of the most recent SPAD arrays include a 240 × 320 array using time-gating (Chan et al., 2019), a 252 × 144 array using shared TDC resources (Zhang et al., 2019) and a 192 × 128 array with in-pixel TDCs enabled by means of an advanced 40 nm technology node (Henderson, Johnston, Mattioli Della Rocca et al., 2019).

The fill factor (FF), the ratio between the active area of the SPAD and the size of the pixel, is an important performance parameter in homogeneously illuminated systems, since only the photons that arrive in the active area of a SPAD can be detected. It is not only that the structure and guard ring of the SPAD need to be designed so that the SPADs can be placed as close as possible to each other but the in-pixel electronics also need to be minimized in order to achieve a high fill factor. The spacing of the active area of the SPAD and the in-pixel electronics will depend on the SPAD structure and the type of electronics used. If the SPAD is formed between a p+ and a deep nwell, only NMOS-type transistors in pwells can be used inside the shared deep nwell. Otherwise additional space will have to be reserved for the nwell needed for PMOS-type transistors and deep nwell separation, which would then lower the fill factor.

The fill factor of a line sensor can be high, since the electronics can be placed next to the line of SPADs and will not affect the fill factor, see Fig. 7 (a). It is difficult to locate the electronics outside the sensor in a large array, however, due to long routing of the signals, which will introduce skews. Also, the fill factor may decrease due to the area needed for the extensive wiring, especially if there are not many metal layers available.

The pixel electronics are usually placed in-pixel, as in Fig. 7 (b), to enable fully parallel operation of the pixel, but either the amount of pixel electronics needs to be small or a low resulting fill factor will have to be accepted, e.g. 3% in (Villa et al., 2014) and 1% in (Veerappan et al., 2011). One option for increasing the fill factor of the sensor is to implement some of the electronics, usually quenching, in-pixel and to divide the area consuming resources between multiple pixels, as in Fig. 7 (c) (Niclass, Favi, Kluter, Gersbach, & Charbon, 2008). When the shared resources (e.g. the TDC) are placed outside the sensor array, they will no longer detract from the fill factor.

To increase the fill factor of the sensor, a 3D implementation has been proposed in which a backside-illuminated (BSI) SPAD array is realized on a separate die and placed on top of the pixel electronics with hybrid bonding (Abbas et al., 2016; Henderson, Johnston, Hutchings et al., 2019). The stacked structure has the advantage of enabling the best technology to be selected for each of the two tiers (Charbon, Bruschini, & Lee, 2018). This solution would obviously result in the best fill factor given a large amount of in-pixel electronics, but one drawback is the increase in complexity and cost.

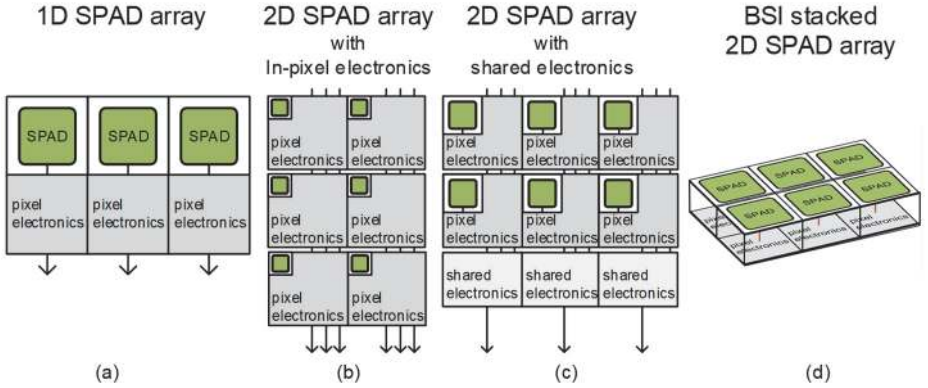

Fig. 7. Placement of the pixel electronics in (a) a line sensor or (b) fully parallel (c) column parallel and (d) 3D-stacked fully parallel structures.

The fill factor can also be increased by including a micro-lens array on top of the sensor array. These custom-designed arrays are able to increase the fill factor, e.g. from 5% to 30% (Burri et al., 2014) or from 13% to 42% (Henderson, Johnston, Mattioli Della Rocca et al., 2019), depending on the layout of the SPAD array and its technology. The additional layer will increase the complexity and cost of the sensor, however, especially as the number of pixels grows larger.

When large arrays are implemented with minimal distances between neighbouring pixels in order to increase the fill factor, cross-talk has to be taken into consideration. When a SPAD is triggered, electrical or optical cross-talk may also trigger the neighbouring SPAD, and this cross-talk will increase with smaller die thicknesses and larger excess bias voltages (Ficorella et al., 2016). The level of cross-talk in mature SPAD technologies is usually negligible, however, so that a cross-talk of <1%, for example, has been measured in an array of 24 µm x 24 µm SPADs with a 45% fill factor implemented in high voltage 0.35 µm technology (Jahromi & Kostamovaara, 2018).

2.3.2 Indirect time-of-flight imagers

Time-of-flight can be measured indirectly by the phase comparison technique (see section 2.2) also in the case of a single photon sensor. An example of a continuous-wave indirect time-of-flight (cw-iTOF) operation principle in which the distance is calculated from the phase difference between the emitted sinusoidal modulated light and the received light signal is shown in Fig. 8, where the phase delay is measured by counting photons in the predetermined time periods Q_1-Q_4 and calculating the phase delay, amplitude and background light from these four samples by means of Fourier transform equations. At least three samples are needed according to the Nyquist-Shannon theorem, but it is common to use four in order to increase the modulation contrast with a reasonable decrease in the fill factor resulting from the increased number of counters in the pixel (Niclass, Favi, Kluter, Monnier, & Charbon, 2009). Phase comparison is used in the pulsed indirect TOF technique (pl-iTOF), but with pulsed active illumination, while the maximum measurable range depends on the length of the laser pulse (Bellisai et al., 2013; Bronzi et al., 2016). The aliasing problem that affects phase comparison in the case of a high frequency continuous-wave signal is the same as was discussed in connection with other pixel types in section 2.2.

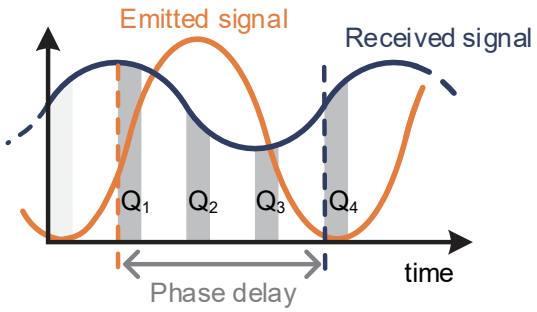

$$\varphi = \arctan\left[\frac{Q_4 - Q_2}{Q_1 - Q_3}\right]$$

$$d = \frac{\Phi\, c}{4\pi f}$$

Fig. 8. Time-of-flight calculated from the phase difference in continuous-wave illumination.

2.3.3 Direct time-of-flight imagers

When time-of-flight is measured directly as the transit time of a short laser pulse, employing a high timing resolution single photon sensor (see Fig. 2), the aliasing problem arising from phase comparison techniques can be avoided. Furthermore,

the width of the light pulse does not limit the measurement range as in the pulsed iTOF technique and short laser pulses can be used to achieve high (even mm-level) precision (Keranen & Kostamovaara, 2019). This section will discuss the operating principle of TOF imagers that use direct time-of-flight measurement and the main challenges involved in designing these.

Operating principle

A direct TOF imager measures the time-of-flight of a laser pulse from the transmitter to the target and back to the receiver directly by using time-to-digital or time-to-analogue converters. The solution is straightforward: the time interval to be measured starts from the moment when the laser pulse is sent and stops when the SPAD is triggered by the echo of the laser pulse, see Fig. 9. Multiple successive measurements are usually needed to distinguish the echo signal from the noise when single photon detectors are used in the receiver. The sensor can also be called a time-correlated single photon counter (TCSPC), as it measures arrival times of single photons synchronized with the laser pulse and collects these into a histogram which has its peak at the distance from the target.

If there is one TDC for each SPAD in a large array, the power consumption can easily increase to a level at which heating becomes an issue, especially when all the TDCs are operating at the same time. When only a small number of SPADs in the array are triggered for each laser pulse, the power consumption can be reduced by starting the time measurement only when a SPAD is triggered and stopping the TDC synchronously with the sending of the laser pulse. In this case the signal indicating the laser pulse will be delayed over the maximum desired time range of the system. In powerful ambient lighting, however, the SPADs are triggered frequently and thus the power consumption of the TDCs remains high even with reverse-triggered start and stop functions in the TDCs. Also, when the photon detection rate is maximized by measuring multiple TDC periods before reading the data from the sensor, the TDC power consumption may eventually become a limiting factor, as noted by (Lussana et al., 2015; D. Perenzoni, Gasparini, Massari, & Stoppa, 2014).

The readout of the timing information of the triggered SPADs from the sensor chip may become a major issue in large arrays. Even an array of 2 kpixels with an 8-bit distance result for each laser pulse at a pulsing rate of 1 MHz would result in an I/O data rate of 16 Gbit/s, for example. Several techniques have been proposed for lowering the I/O data rate, e.g. event-driven readouts (Niclass et al., 2008),

region-of-interest readouts (Veerappan et al., 2011) or histogramming on-chip (Zhang et al., 2019), but it must be admitted that the speed of measurement in large arrays is still often limited by the I/O data rate.

The placement of the pixel electronics in direct TOF imagers needs to be designed carefully, since the better the TDC resolution and range are, the larger is the area needed for the electronics, which may lead to a low fill factor if one TDC is employed for each pixel, as discussed in section 2.3.1. One TDC for a group of pixels would be a good solution when the ratio of the photon detections in the SPADs is low and when it is unlikely that more than one SPAD in a group will be triggered at the same time (Portaluppi, Conca, Villa, & Zappa, 2019).

Pile-up distortion

When the number of photons from the echo of the laser pulse at the receiver is low (detection probability <<1), multiple laser pulses need to be sent and a histogram of the detected photons should be constructed after successive measurements. See the illustration in Fig. 9 (a) of the construction of the histogram when neither the noise nor the background triggers the SPAD.

Under conditions of powerful ambient lighting a single photon sensor will detect photons arriving from ambient light sources, e.g. a lamp or the sun, and if the SPAD is already triggered by this noise, the signal echo may be blocked out, see an illustrative example of such a histogram in Fig. 9. (b). There are two mechanisms that may cause pile-up distortion and eventually block echo signal detection in a TDC-based structure: one is the conversion time of the TDC and another is the dead-time of the SPAD. This issue is especially prominent in systems where there is only one TDC channel per SPAD pixel, since in this case only one detection can be recorded per transmitted laser pulse. If the TDC has been triggered by noise, a certain dead-time has to elapse until the next measurement (in the worst case a whole laser pulsing period). The net effect is a lowering of the probability of detection by the signal photon and thus a reduced SNR for detection. This problem is sometimes referred to as pile-up distortion, since it piles the photons up in the first bins of the histogram, as illustrated in Fig. 9 (b).

Methods are available for correcting distorted histograms (Coates, 1968) but these do not prevent the echo signal from being masked by the noise. Pile-up distortion is recognized in LiDAR systems and also in spectroscopy (Harris & Selinger, 1979), and numerous solutions to this problem have been studied.

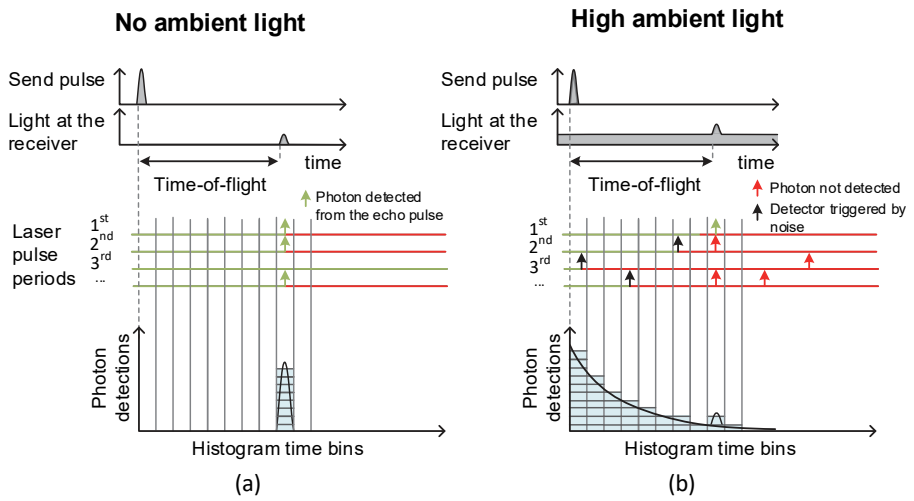

Fig. 9. (a) Direct time-of-flight technique. (b) The echo signal from the target will be blocked due to high ambient light in the SPAD sensor unless preventive measures are adopted.

Attenuation of the photon detection probability has also been studied as a means of preventing the blocking of echo signals due to high ambient light (Gupta, Ingle, Velten, & Gupta, 2019). As the sensitivity of the sensor decreases it will become more likely that the SPAD will fail to be triggered on account of ambient light and will be active at the time when the echo of the laser pulse arrives. Attenuation of the PDP should be considered for each SPAD separately and in an adaptive manner, i.e. depending on the photon detection rate of ambient light at the receiver, since otherwise signal detection from low reflectivity targets may decrease below the detectable level. The PDP could be lowered by changing the biasing of each of the SPADs independently, for example, but the circuit complexity at the sensor would increase and additional signal processing would be needed to define the necessary biasing for each pixel.

Another solution for reducing the conversion rate of the photons arriving from background lighting would be to use photon coincidence detection (Niclass et al., 2013; Niclass, Soga, Matsubara, Ogawa, & Kagami, 2014; M. Perenzoni, Perenzoni, & Stoppa, 2017). In this technique a group of SPADs is assigned to one TDC, which records the photon detection only when two or more SPADs in the group have been triggered within a certain pre-determined coincidence time. This technique increases the measurable range in powerful ambient lighting depending

on the number of coincidences and the coincidence time (Haase et al., 2019) but also detracts from the sensor spatial resolution if the positions of the triggered SPADs in the macro-pixel are not stored. Also, the photon coincidence detection should be adjusted adaptively in order to achieve high performance for both low and high-reflectivity targets (Beer, Haase, Ruskowski, & Kokozinski, 2018). Most importantly, the use of these techniques inherently necessitates the detection of more than one photon within the correlation window, which is seldom the case in practical applications due to transmitter energy limitations.

One option for reducing the blocking of the echo signal due to unavailable TDC resources is to use a time window, which enables the TDC to operate only if a passively quenched SPAD is triggered within a predetermined time (Henderson, Johnston, Mattioli Della Rocca et al., 2019). Under conditions of powerful ambient lighting, however, passively quenched SPADs will be triggered frequently, resulting in considerable power consumption.

Another solution for preventing the blocking of the echo by background light is to use a time gate for the SPAD, so that its activation is delayed relative to the laser pulse, since a SPAD that is not activated cannot be triggered by noise sources. If multiple time periods (time gates) are used for activating the SPAD it may even be possible to measure long ranges in spite of high ambient lighting (Kostamovaara et al., 2015).

3 A time-gated SPAD array for 3D range imaging

In this work a solid-state time-of-light imager for 3D range imaging applications has been developed which measures distances from 2000 points (in this specific realization) by sending a short, energetic laser pulse to illuminate the scene (FOV) and measuring the times-of-flight of the photons of the laser pulse by sampling the state of a SPAD array sequentially in predetermined time windows. The sampling of the SPAD array is realized by means of "adaptive" sliding time-gate techniques, the operating principle of which is described in section 3.1. Moreover, the SPAD array was divided into subarrays in which the time-gating positions could be independently controlled. The principle of frame rate improvement by dividing the array into subarrays is presented in section 3.2. To show the feasibility of the system for real-time applications, an FPGA-based interface and algorithm were also developed, as described in section 3.3.

3.1 A solid-state imaging system using short laser pulses and a sliding time-gate technique

The solid-state time-of-flight imager operating with short, energetic laser pulse illumination had a positive lens system installed in front of the detector and a SPAD array to form the desired field of view for the receiver, see Fig. 10. A diffuser was then used to spread the energy from the laser beam to match the active illumination with the field of view of the receiver. The time-of-flight of the laser pulse can be measured by different methods, i.e. directly or indirectly, as described above, and in this case a time-gating approach in which the sensor is activated with a certain time delay relative to the laser pulse was used. The width of the time gate was reduced to a minimum and the technique used not only to filter the noise but also to determine the time-of-flight of the recorded photon.

The sensor is a SPAD array, the state of which (pixel detection or no detection) is sampled with a predetermined delay relative to the laser pulse, so that the time-of-flight of the laser pulse is determined from that time-gate position within the histogram of collected results that contains the maximum number of photon detections. The distance from the target can be calculated from the time-of-flight (t_{TOF}) of the laser pulse, since the speed of the laser pulse is known (c = the speed of light).

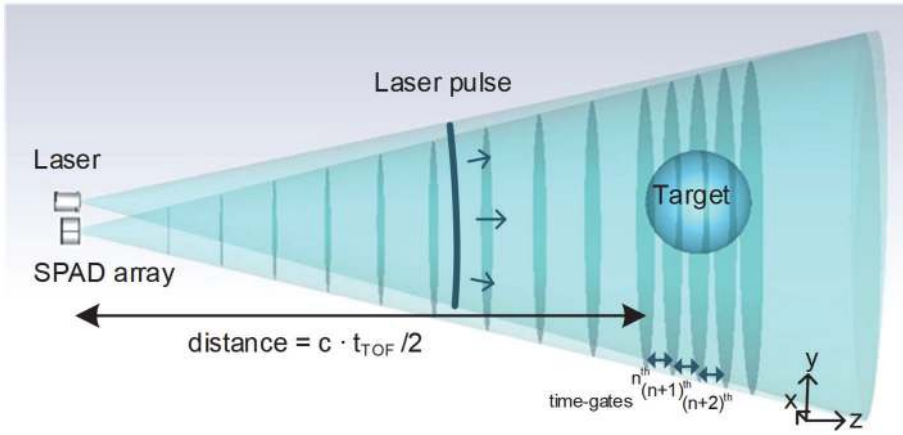

Fig. 10. The solid-state imaging system with a pulsed laser and a time-gated SPAD array, c = the speed of flight (modified from Paper I).

An artistic representation of the time-of-flight calculation based on the sliding time-gate principle that is used in this work is presented in Fig. 11 which demonstrates the determination of a flight time from a histogram with ideal time-gates of 0.5 ns, 1 ns or 2 ns which are used to activate a SPAD and sample the photons arriving at the detector. The figure shows that the time gate should be minimized (matched with the width of the laser pulse) in order to reduce noise and ensure that the echo of the laser pulse is located in the smallest number of histogram bins. This also has an impact on the frame rate, as discussed below.

To speed up the distance measurement, the scanning steps could be limited to the range of interest, i.e. the area around the target surface, which can be defined as a predetermined distance range, for example, or, as in Fig. 11, in terms of the time-gate positions which have detected an echo signal. If the latter can be done the frame rate will increase considerably compared with the situation in which the whole measurement range needs to be scanned, since the range of interest can be shifted "adaptively" as the target moves back and forth, for instance.

By using a technique in which the opening of the SPAD is delayed by a predetermined step relative to the laser pulse, as in this work, the blocking of the echo signal due to the pile-up effect of ambient light (see section 2.3.3) can be avoided. Also, the receiver IC will be fairly simple if only ON-OFF sampling of the SPAD array at a certain interval after the laser pulse is needed. The simplicity of the pixel electronics paves the way for a high fill factor, and also makes it easier to scale up the total area of the receiver if necessary. Also, the amount of data to be

read out from the sensor IC is low, since the timing information is already known and only the result, whether the SPAD was triggered or not (1 bit/SPAD), has to be transferred.

Since the time gate position for which the photons are counted is predetermined, the peak which defines the time-of-flight can be detected as the scanning proceeds and the full histogram does not need to be saved. Hence the memory resources needed are greatly reduced compared with TDC-based systems, in which the timing of the triggering of each photon has to be saved in a histogram before starting the peak detection procedure. The memory size needed for 2000 pixels with an 8-bit depth resolution and 8-bit maximum photon counts would be 4 Mbits, which can be compressed by a factor of 25-to-1 if only 10 histogram bins are saved, for example.

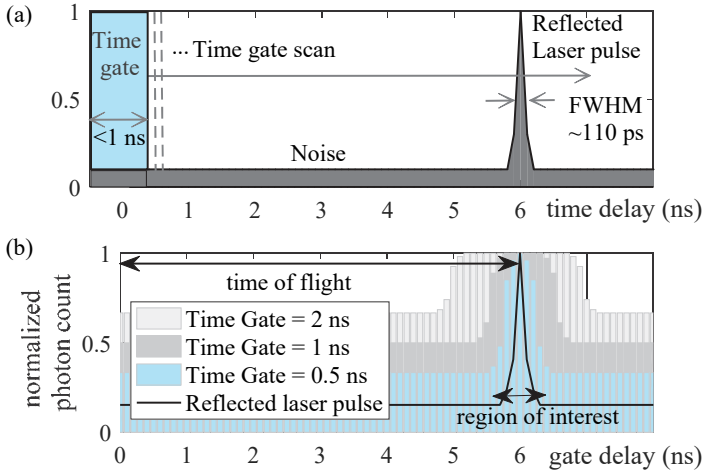

Fig. 11. Determining the time-of-flight of a short laser pulse by sliding a time-gate of 1 ns in 100 ps steps (Reprinted by permission from paper III © 2019 IEEE).

3.2 Dividing the 2D SPAD array into subarrays with independently controlled time-gating

If there were only one time-gate signal controlling all the SPADs in an array, the scanning range would have to be wide enough to include the target surfaces seen in all the pixels of the array, see Fig. 12 (c). By dividing the array into independently controllable macro-pixels (sub-areas), the time-gating signals of the SPADs in

different sub-areas can be set to different time positions independently of each other, see Fig. 12 (b). This makes it possible to divide the system field-of-view (FOV) into multiple sub-FOVs, see Fig. 13, all of which have their own scanning ranges, i.e. regions of interest. Hence different parts of the receiver could be set to measure targets at different limited scanning ranges at the same time. It is important to note that while this is happening individual SPADs within the sub-area can still give results independently of each other (limited only by the length of the sub-range).

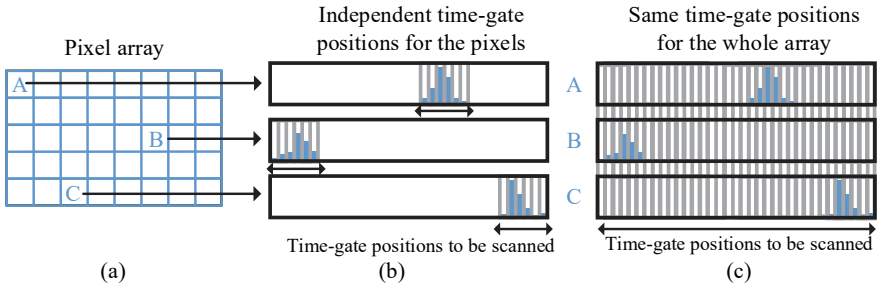

Fig. 12. Examples of histograms of photons counted from a laser pulse echo, (a) in pixels A, B and C at time-gate positions when (b) the array has multiple independently controllable time-gating signals, or (c) there is one time-gating signal for the whole array.

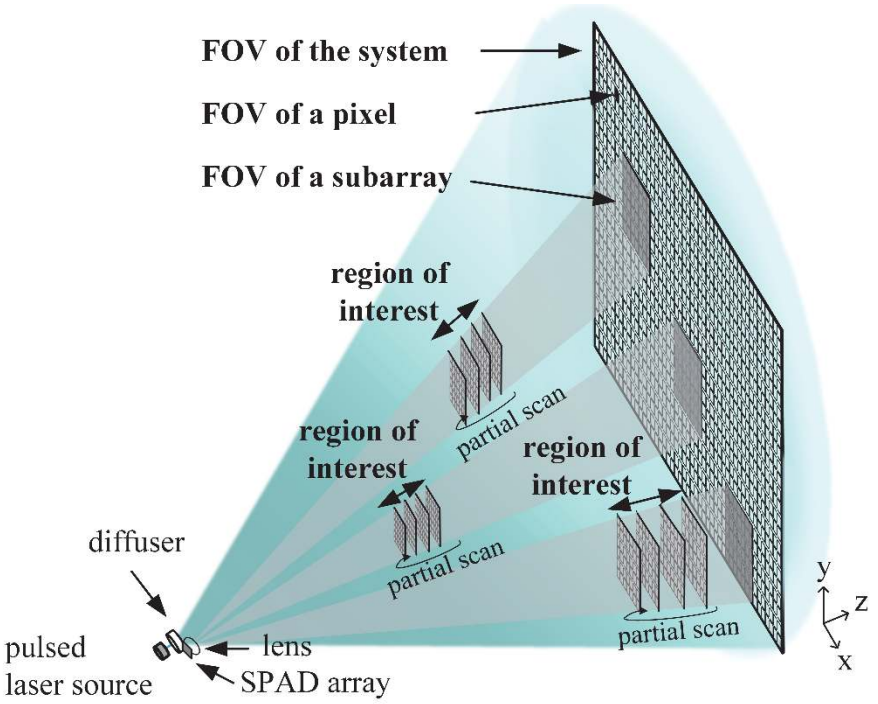

Fig. 13. By dividing the receiver SPAD array into sub-arrays, the scanning of the range of the system FOV can be divided into multiple regions of interest that are located at different distances (Reprinted by permission from Paper III © 2019 IEEE).

3.3 Adaptive scanning of time-gates depending on the distances of the moving targets

An algorithm that sets the time-gating positions in a manner dependent on the detected target position has been developed in order to demonstrate the feasibility of the system in real-time applications (Paper IV). The aim of this FPGA-based digital design was to demonstrate how the scanning ranges of the subarrays can be minimized (to achieve a higher frame rate) and how the surfaces of a moving object can be traced. Not only does the frame rate of the measurement have to be fast but also the next time-gate positions need to be determined quickly in order to be able to follow a moving target (especially when it moves transversally within the system

field of view from one subarray's FOV to another, since otherwise the echo signal can be lost and in worst case the full range has to be scanned again.

Fig. 14 shows the principle of an algorithm in which the scanning of a range consists of a few steps which are first scanned (scan 1, the time-position of which could be based on knowledge of the target position determined in an earlier tracking phase) and the next scanning range (scan 2) depends on the detected echo signals measured in the first scanned range. If a valid echo signal is detected within the sub-range, the next scanning range (scan 2) will remain around the target, as in ROI 1 in Fig. 14. If no echo signal is detected, scanning will continue further away until a valid echo signal from the target has been detected, as in the subarray in the middle of the array in Fig. 14. When a target is moving away from the detector the echo signal will be delayed and if the target is moving towards the detector the signal will be advanced and the movement can be detected simply by setting the next scanning range around the echo signal in each measurement. The frame rate of the limited scanning range obviously needs to be high enough to keep up with any movement that takes place.

It is not enough, however, to follow the movement of the target in the direction z alone, as spatial movement on the plane xy also has to be taken into account. Otherwise a problem would arise if a target were to move sideways from the field of view of one subarray to that of another where the limitation of the scanning range is such that it is not possible to detect the new echo signal coming into its sub-field of view. In order to be able to address this problem and catch an echo signal even after possible xy movement of the target, an echo signal coming into the FOV of the subarray from the side should also be taken into account when determining the next scanning range. Thus, if any detections are seen in the adjacent pixels of the subarray (i.e. around its perimeter), these can be used when selecting the next scanned sub-range. This is illustrated in Fig. 14 by the case of ROI 2, the next scanning range for which (scan 2) jumps to the location where the target has been detected in an adjacent pixel in the subarray.

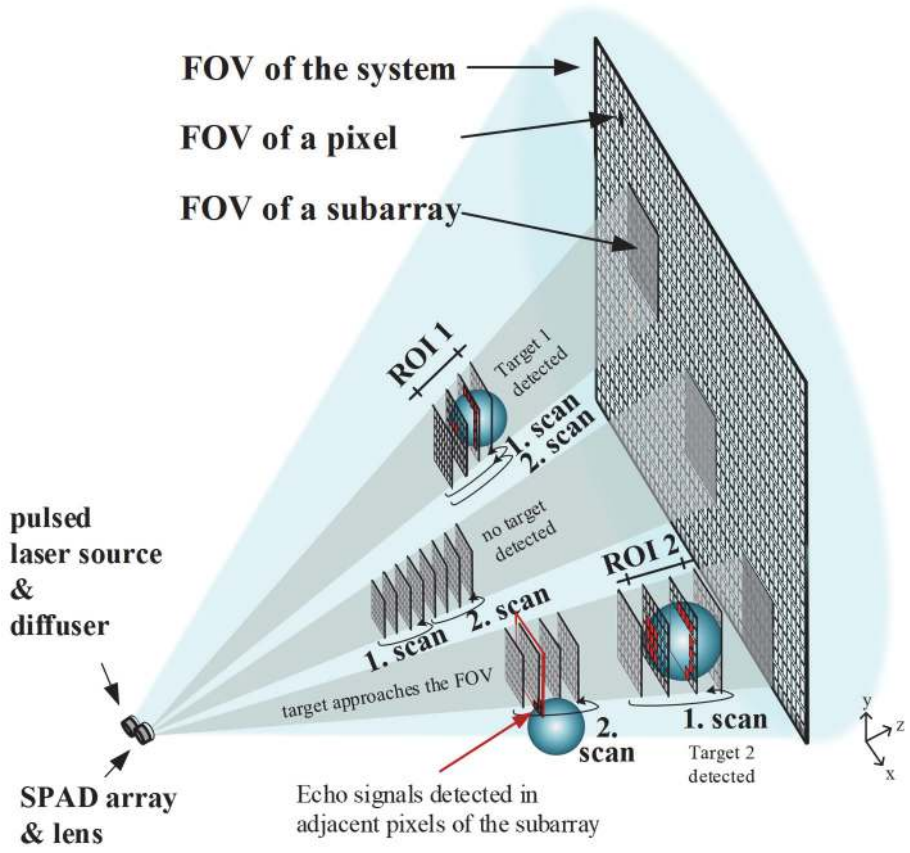

Fig. 14. Principle for selecting scanning ranges for subarrays (Modified from Paper IV).

In some gesture control applications the range for a subarray of pixels, for example, can be limited to the nearest target and it is enough to scan the distances only around the nearest surface to the imager. When the range is tightly limited to the nearest surface, however, the other pixels in the subarray that see a target within their FOV lack signal detections if the target is further away than the scanning range. This problem can be solved by adding multiple partial scanning ranges for the subarray so that all target surfaces within the sub-FOV of each subarray will be scanned. If the scanned sub-range is limited to one interval of 21 cm, for example, by adding another 21 cm sub-range at a different distance, two independent ranges of interest can be recorded, as shown in Fig. 15.

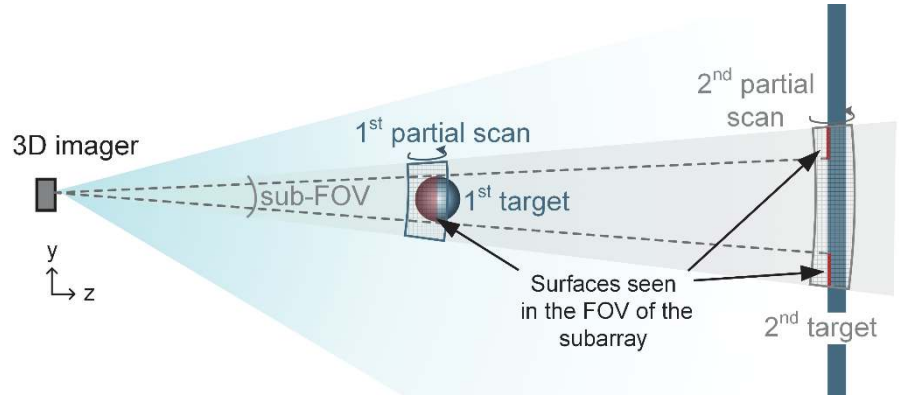

Fig. 15. Two partial scanning ranges implemented for one subarray.

This novel time gating approach which allows adaptive gating **in both the time and space domains**, together with its practical realization in a CMOS technology, can be regarded as the **key contribution of this thesis**.

4 Electronic design of the SPAD array chip

An 80 × 25 SPAD array chip with time-gating circuitry was designed in order to be able to study how the sliding time-gate technique with adaptive time-gating control described in the previous chapter could be applied to 3D range imaging. The details of the electronic design were published in Paper III, and the main features and results are summarized in this chapter. The architecture of the chip is described in section 4.1, the details of the pixel electronics are shown in section 4.2 and the on-chip time-gating circuitry is presented in section 4.3. The main characterization results regarding the SPAD array are presented in section 4.4. The controlling of the time-gating signals by means of an FPGA-based algorithm is briefly described in Paper IV. This algorithm is described here in section 4.5, together with certain improvements that have been developed since the publication of Paper IV.

4.1 Architecture of the chip

An array of 2000 pixels was designed in order to study the functionality of the ideas presented in the previous chapter. The routing of signals to the centre of a large array can be difficult, and either the fill factor needs to be reduced on account of the limited routing channels or else a compromise has to be reached regarding the simultaneous operation of the SPADs. In this case the states of the SPADs are saved in in-pixel registers at the trailing edges of the time-gates and the result can be read out from the array by connecting the registers in series. This minimizes the number of routing channels needed to read out the result.

Each pixel has one SPAD and its electronics to sample, whereupon the sampled state is saved in the pixel and also for loading the SPAD well above the breakdown voltage (the leading edge of the time-gate). In order to be able to implement short time-gating for the SPAD, it is beneficial to transfer the timing signals as “rising edges” that are combined into short pulses only in the pixel, especially if the routing wires are long (e.g. 2.5 mm in the prototype). Thus three rising edges (two for loading and one for sampling the SPAD) are needed for the time-gating of each SPAD. A more detailed description of the pixel electronics is presented in section 4.2 below.

The SPADs are combined into sub-groups of pixels, sub-arrays of 50 SPADs that share the same time-gating signals, so that the transferring of three time-gating signals for each pixel would not detract from the fill factor. This arrangement also reduces the amount of control electronics. The system was developed for use in

applications where distances are measured from surfaces (e.g. gesture control, in which the distance result changes fairly smoothly between adjacent pixels in many cases), so that subarrays of pixels are also justified from the system perspective.

The chip has 2000 SPADs that are divided into groups of 50, resulting in 40 subarrays. The timing circuitry has been implemented on-chip in order to meet the aims of the study, i.e. control over the time gating of tens of subarrays separately with the shortest possible routings of the signals and a reasonable number of I/O pins. The block diagram of the SPAD array chip is shown in Fig. 16.

The time-gating signals are arranged to cover a time range of 24 ns (corresponding to a distance range of ~3.6 m). The delay grid is ~100 ps (~1.5 cm), in order to detect human movements, for example. The time-gating signals are provided by a DLL block that includes delay lines locked into a reference clock. The choice for the time-gating signal positions is written into a serial-in-parallel-out (SIPO) register that controls a multiplexer (MUX), which then passes the selected DLL block output through to the SPAD subarray. Three time-gating signals are transferred to each of the 40 subarrays, resulting altogether in 120 SIPO registers and MUX chains.

The DLL block provides the timing grid not only for the time-gating signals but also for the laser trigger signal, making 120 rising edges available for choice as the laser triggering signal and 240 edges as time-gating signals. The DLL block consists of two similar delay-locked loops, at least one of which needs to be powered for the sensor to operate, and both if a denser delay grid is needed.

A photograph of the SPAD array chip showing the placement of the main blocks is presented in Fig. 17. The size of the chip is 5.02 mm x 5.69 mm, of which the active sensor area takes up about 35% (4 mm x 2.5 mm).

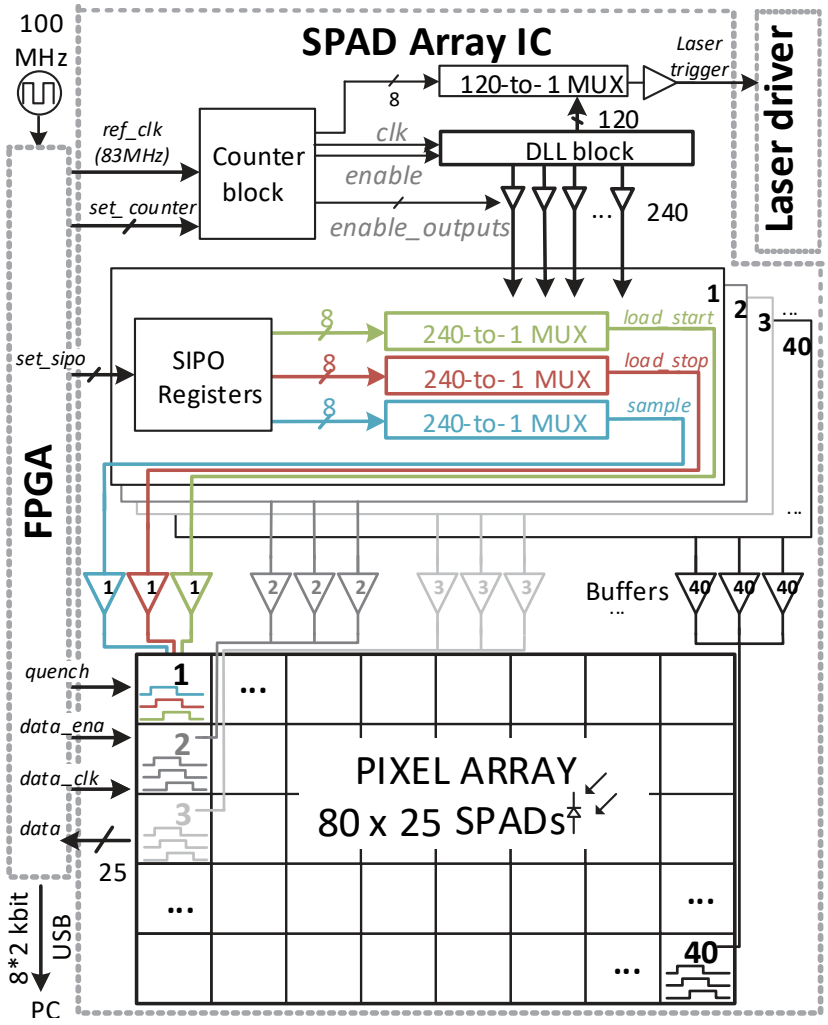

Fig. 16. A Block diagram of the SPAD array chip (Reprinted by permission from Paper III © 2019 IEEE).

The timing diagram of the system is presented in Fig. 18. The length of the delay line of the DLL block is 24 ns, which is also the maximum time by which the time-gating signals in the various sub-groups can differ from each other. In order to be able to set the delay of the time-gating signals further away from the triggering of the laser pulse than 24 ns, a counter has been included on the chip to enable outputs from the DLL block to occur after a predetermined integral number of 24 ns

periods. The triggering signal for the laser pulse that is sent from the SPAD array chip to the laser driver circuitry can be adjusted within 24 ns on a grid of 200 ps in order to shift the time-gating of the SPAD array to match the range of the target or to compensate for the latency of the laser driver circuitry.

After the states of all the SPADs in the array have been sampled by means of the trailing edge of the time-gate signal, the in-pixel registers are connected in series, resulting in multiple 80-bit registers which can be read out from the chip with the aid of 25 I/O pins. The choice to read the data out directly from the chip (as opposed to on-chip post-processing) was made since this enabled us to study the system with the full flexibility provided by the FPGA and software-based post-processing. The system clock frequency was set to 83 MHz, which limits the maximum laser pulsing frequency to 1 MHz when 80 cycles are needed for the readout and 3 cycles are reserved for sampling the state of the SPADs.

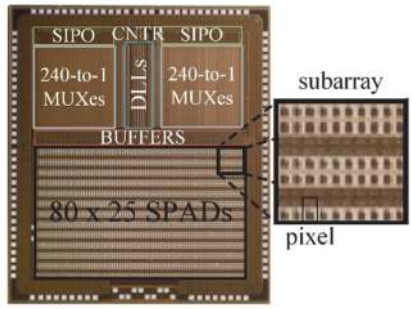

Fig. 17. Layout of the SPAD array chip (Reprinted by permission from Paper III © 2019 IEEE).

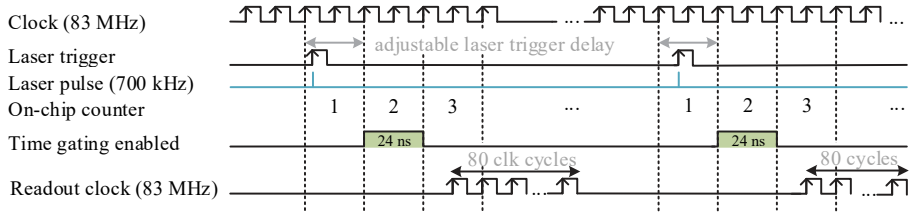

Fig. 18. Timing diagram of the operation (Reprinted by permission from Paper III © 2019 IEEE).

The power consumption of the SPAD array chip is mainly taken up by the data readout and the DLL block. The measured average current consumption at a pulsing rate of ~1 MHz was 172 mA when both DLLs were operating and 167 mA when

only the primary DLL was active. The average current consumption of the readout was about 150 mA and will decrease with any decrease in the pulsing rate, resulting in average current consumption of 15 mA with a pulsing rate of 100 kHz. The current consumption of the DLL block can be reduced from the always-on situation by gating the reference clock. For a pulsing rate of 100 kHz, for example, a current consumption of 5 mA was measured when both DLLs were functioning and 3 mA with only one DLL on. In this configuration, the DLLs were activated 1.2 µs before each measurement. The power consumed for writing into the SIPO registers (setting the time-gate position) is negligible since more than a hundred, or even a thousand, measurements are usually made for each time-gate position and the SIPO registers need to be re-written only when the time-gating signals are changed.

4.2 Pixel electronics

In order to achieve a high fill factor for the sensor part of the chip, the in-pixel electronics should be minimized. Each pixel consists of a SPAD, time-gating switches for the SPAD and one bit of memory storage. A schematic diagram of the pixel electronics is presented in Fig. 19.

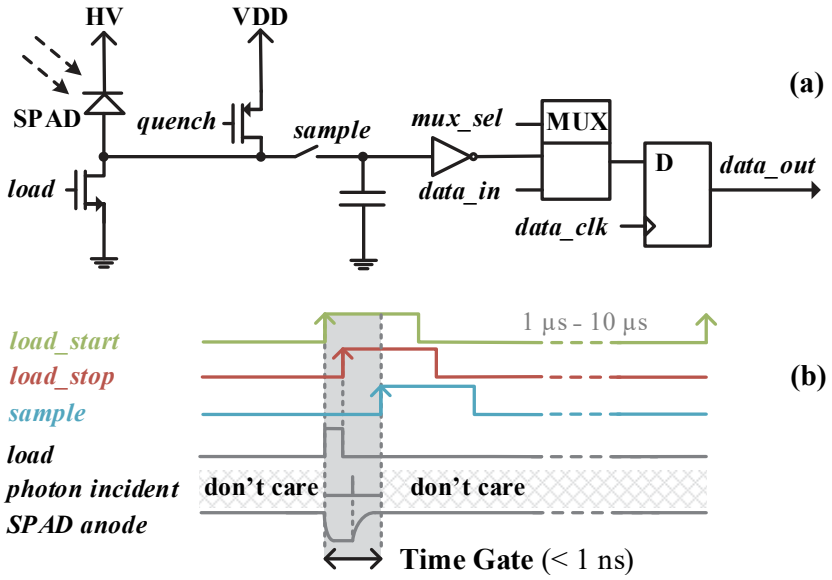

Fig. 19. Schematic and timing diagrams of the pixel electronics (Reprinted by permission from Paper III © 2019 IEEE).

The time-gate window (active detection period) starts when the SPAD is loaded above the breakdown voltage, which is the region where the SPAD is active and able to trigger even from a single photon. The time-gate window ends when a sample of the state of the SPAD is taken with the *sample* signal. The state of the row of 80 SPADs is then read out from the array by connecting the in-pixel registers (D) in series with multiplexer (MUX).

Each SPAD is realized between p+ diffusion and deep nwell with pwell guard rings, a construction which has also been used in many other studies (M. Perenzoni et al., 2016). The active area of a SPAD is 36 µm x 44 µm, resulting in a fill factor of 32% for the pixel (calculated from the layout). The SPADs are rather large in size compared with the figures usually reported (~20 µm or less in diameter), since the use of short time-gates allows a higher dark count rate for the SPADs. Also, the goal was to use the SPAD array in imaging applications where there is usually some ambient light present, e.g. from a lamp or daylight, whereupon the random hits produced by the background could easily dominate over the DCR. The SPAD cathode is connected to the high voltage (HV~22 V) node and the anode is connected to the voltage supply (VDD=3.3 V) before activating the SPAD. A row of SPADs is implemented in a same deep nwell, resulting in a significant increase in the fill factor due to the large guard rings needed between the deep nwell structure and the electronics implemented on the substrate.

The chip is designed for a 0.35 µm high voltage (HV) technology, which provides adequate performance for the SPAD. This technology was chosen on the grounds of the research group's prior knowledge of the SPADs in this technology.

4.3 Circuits for implementing on-chip time-gating

The time-gating signals for the SPADs were selected from the outputs of an on-chip DLL block with 240-to-1 MUXes. This section will present the DLL block design together with measurements of the linearity of the time gating signals.

4.3.1 DLL design

The DLL block consists of two similar delay-locked loops (DLLs) which are driven by complementary clock signals. The primary DLL is always used when the chip is operating and the secondary DLL when the timing grid needs to be increased. The operating principle and structure of a DLL block are illustrated in Fig. 20.

The DLL consists of a delay line, phase detector and charge pump. The length of the delay line is 24 ns when it is locked to a 83.33 MHz reference clock divided into two. The reference clock is divided on-chip in order to provide the DLLs with precisely inverted input signals. Since one delay line consists of 119 delay elements, the timing grid of the output signals is 202 ps.

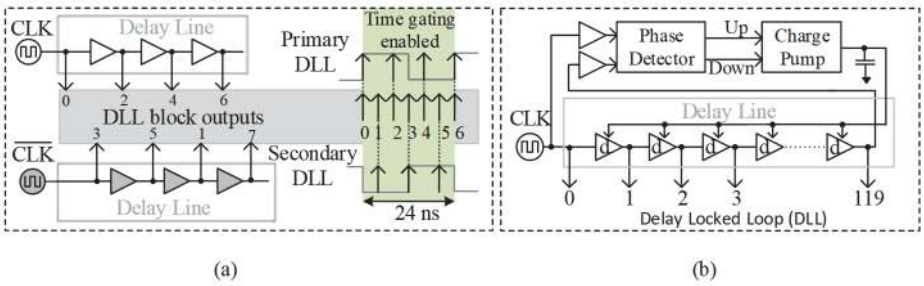

Fig. 20. (a) Generation of DLL block outputs. (b) Structure of a DLL (Reprinted by permission from Paper III © 2019 IEEE).

4.3.2 Linearity of the on-chip time-gating

The linearity of the time-gating signals was measured with a test circuit that drives the signals to the printed circuit board (PCB) from the left-most column of the array (see Fig. 17). The linearity results include both the linearity of the 240 outputs of the DLL block and the linearity of the 240-to-1 MUX chain. The results show an integral non-linearity (INL) of ±100 ps up to the histogram bin 187 and an increase to ± 200 ps after that, see Fig. 21. The reason for the increased non-linearity was found to be due to multiple simultaneous digital events and parasitics in the power supply lines.

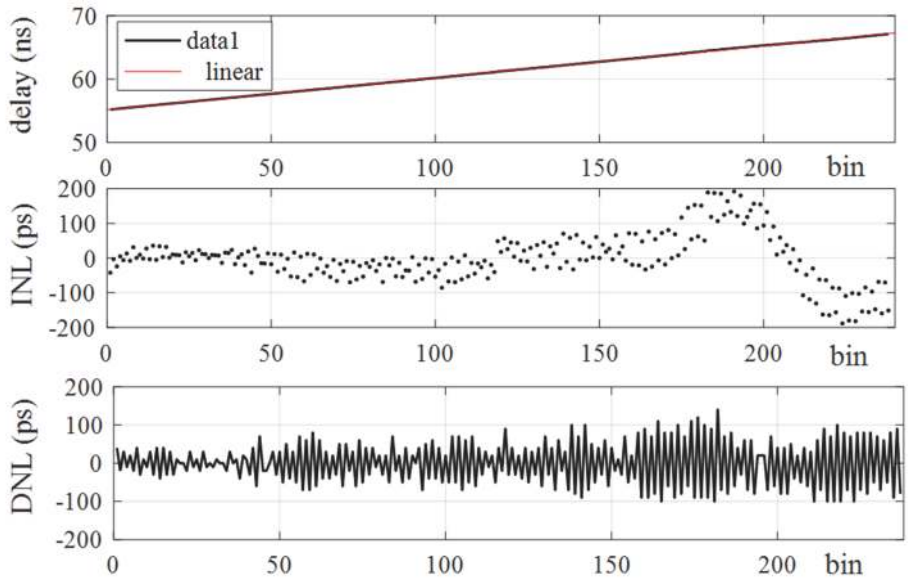

Fig. 21. Linearity of the time-gating signals (Reprinted by permission from Paper III © 2019 IEEE).

4.4 Array characterization

Measurements of the dark count rate (DCR) and the uniformity of the time-gating of the SPAD array are shown in this section.

4.4.1 Noise measurement

The intrinsic noise in the SPAD arrays, the dark count rate, is measured by calculating the SPAD triggerings that take place in the dark. The measured median dark count rate of the SPAD array is ~200 kHz, 122 cps/μm^2, at a bias voltage of 22 V, see Fig. 22. The DCR is higher than is typical in SPAD arrays targeted for applications with low background illumination. As already pointed out, the current system is targeted for brighter ambient lighting conditions, where random background photons typically dominate in the noise, and thus the fill factor is increased by increasing the active area of the SPAD to achieve better photon detection efficiency at the expense of increased DCR.

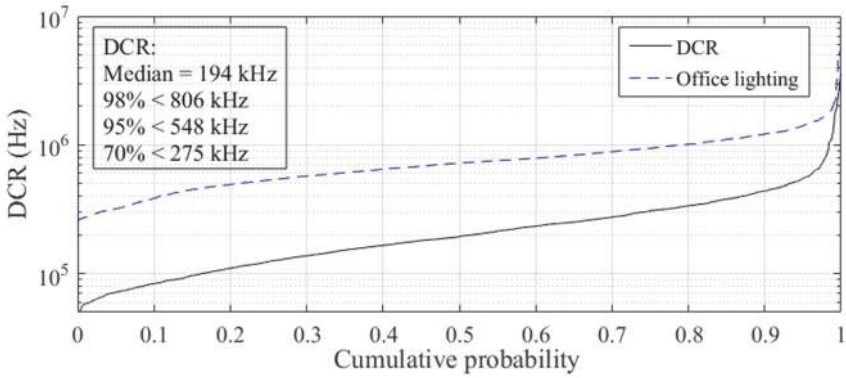

Fig. 22. Cumulative dark count rate of the array (Reprinted by permission from Paper III © 2019 IEEE).

4.4.2 Time-gating

The uniformity of the width of the time-gate across the array was measured with two time-gate settings. Median time gate widths (full width at half maximum, FWHM) of 400 ps for the 0.8 ns setting and 620 ps for the 1 ns setting were measured, see Fig. 23. The laser pulse width used in these measurements was FWHM ~110 ps. The variation in the width of the time-gate from one pixel to another is most likely to be caused by the skew in the signal lines and a non-ideal distribution of the power supply.

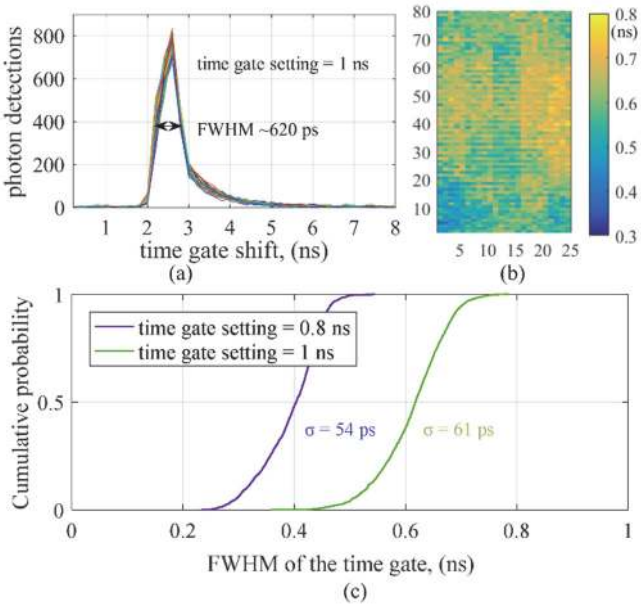

Fig. 23. Per-pixel time gate width variation (FWHM) (Reprinted by permission from Paper III © 2019 IEEE).

The width of the time gate should be minimized in order to reduce noise, and the effect of doing this was demonstrated with three time-gate settings. The result obtained for one pixel in the middle of an array using a white paper target perpendicular to the imager system is shown in Fig. 24, where it can be seen that the shorter the time-gate is, the fewer noise triggerings are detected. More accurate determinations of the signal position are also obtained with a shorter time gate.

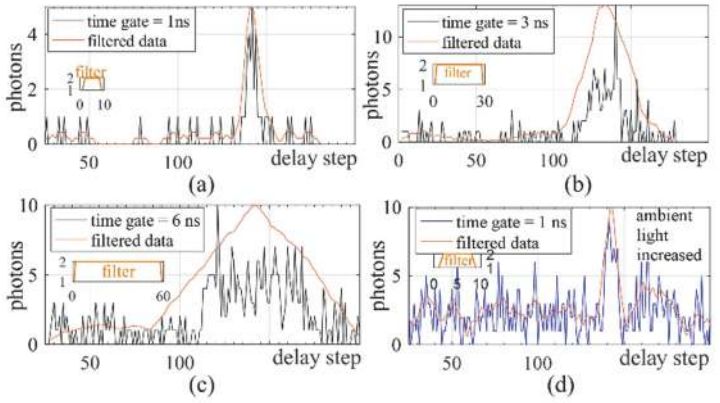

Fig. 24. Effect of the width of the time gate on the detection histograms with office lighting of ~200 lux. The time-gate widths are 1 ns, 3 ns and 6 ns in a, b and c, respectively. In (d) the time gate width is 1 ns and the ambient light has been increased to ~600 lux with halogen lamps (Reprinted by permission from Paper III © 2019 IEEE).

It can be seen from Fig. 24 that when the time gate is shorter the time during which the SPAD is activated is also shorter, and consequently the effect of noise is smaller. Also, the signal is located in fewer bins, which leads to a faster frame rate, since only the bins around the target (in the range-of-interest) need to be measured.

4.5 Controlling the scanning of the ranges of the subarrays

The SPAD array chip is controlled with a field-programmable gate array (FPGA) which reads the data from the integrated circuit (IC) and sets the time gate positions for the next measurement. The digital design implemented in FPGA has gradually evolved during this PhD project, and some improvements have also been added since the publication of Papers I-IV, e.g. the maximum laser pulsing rate has been increased from 700 kHz to 926 kHz and the laser pulsing rate can now be either 100 kHz, 700 kHz or 926 kHz. In addition, a setting that enables **a second partial scanning range** for each subarray within the same measurement cycle has been implemented as a new feature. The reason for this has already been explained in section 3.3. Details of its implementation will be presented later in this chapter and its impact on performance is demonstrated in section 5.2.

The laser pulsing rate is controlled from the FPGA that counts the clock cycles of the system clock (83.33 MHz) and sends a signal to the SPAD array IC when a laser pulse should be sent. The pulsing rate can be selected to be 100 kHz, 700 kHz

or even up to 926 kHz depending on the speed and power consumption requirements of the system. A block diagram of the FPGA design at a pulsing rate setting of 700 kHz is shown in Fig. 25.

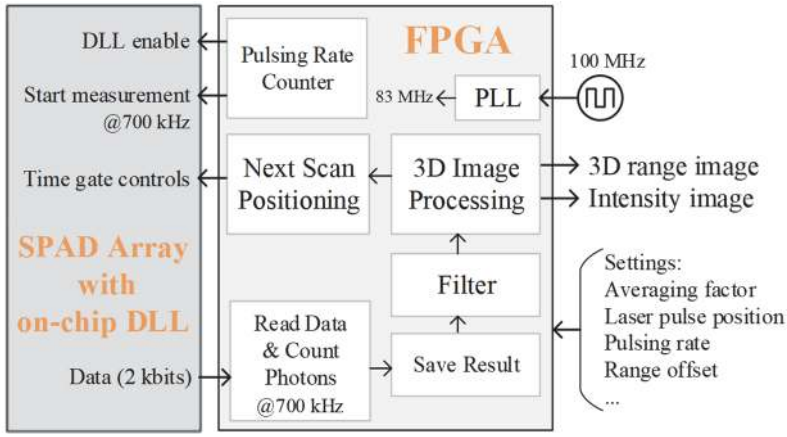

Fig. 25. Simplified block diagram of the control of the SPAD array (Reprinted by permission from Paper IV © 2019 Society for Imaging Science and Technology).

Since the photons are counted for one histogram bin per laser pulse, the algorithm is designed in such a way that the histogram data are filtered using a FIR filter in the FPGA as the scanning proceeds. The maximum of the filtered bin result is taken as the position of the target, and is then transferred to the PC through a USB connection.

The range of the depth measurement is determined by the FPGA, which controls the time-gating positions of the SPADs. The partial scanning ranges can be selected to be 21, 30 or 60 cm and the resulting number of time-gate positions depends on the desired range and on the time-gate shift, which can be selected to be either 101 ps or 202 ps (corresponding to 1.5 cm or 3 cm).

The frame rate depends on the number of scanning steps needed for each frame, the number of laser pulses used to collect the histogram data and the pulsing rate of the laser. These variables are set by the user and depend on the target scene and performance requirements.

After each partial scanning range has been recorded with the desired number of laser shots, the shortest distance results for each of the subarrays can be determined. Next a partial scan is set up around the shortest distance result gained from the previous measurement. If there were no distance results in the subarray,

the next partial scanning range will continue from the previous position further towards the maximum range until the full predetermined measurement range (24 ns) has been scanned.

In order to follow the spatial movement of the target (in the plane xy) not only the pixels in the subarray but also the adjacent pixels of the nearest other subarray should be taken into account when deciding the next scanning range. In the prototype the adjacent pixels are limited to one row on each border of the subarray, since to maximize the frame rate the limited scanning of the range has to be aimed tightly around the target surface and should shift only when the target is on the border of the subarray's FOV.

Since partial scanning of the range is limited to predetermined range selections of 21, 30 or 60 cm, a feature that enables a second partial scanning range for the subarrays, is also implemented. If the partial scanning range is shifted because a new target has come into the FOV of the subarray, the second scanning range will remain at the distance of the background, for example (see Fig. 15). If adjacent pixels in a subarray have distance results that are further away than the first partial scanning range, another partial scanning range must be set in that position. If all the signal detections are within the first partial scanning range, the second partial scanning range should extend the range further away from the receiver. The drawback with a second partial scanning range is that the frame rate of the system is reduced by a factor of 2 when the setting for two partial scanning ranges is selected, since the second partial scanning increases the number of scanning steps needed by two.

The above approach necessitates that the target surface should be found first, before the scanning can be set at the area around the surface. In the prototype the find phase is shortened by setting the positions of the time gates of the subarrays at the beginning of the operation in such a way that they probe a longer distance range (see the convex shape of the beam in Fig. 26 (a)). The time taken to find a target depends on the range of the target and the frame rate (FR) and partial scanning range (PSR) settings. At FR=70 fps and PSR=30 cm the speed of the scanning is 21 m/s (speed=FR·PSR), for example. When the echo signal from the target has been detected, the partial scanning range will be set around the surface range.

Another option for finding a new target would be to first scan the full range and if no target has been detected, a limited scanning range could be set to wait for a new target at the edges of the scanned range. In this way, the find phase can be shortened if a new target is able to enter the field-of-view of the imager only at a known distance, e.g. when the imager is placed in the corner of a room, see Fig. 26

(b). An echo signal from a new target can also be detected rapidly if the partial scanning ranges can be set to optimal application-specific locations. Fig. 26 (c) shows an example of the positions of limited scanning ranges of the prototype's subarrays optimized for waiting for a new target to appear on the scene at a distance of ~3 m. However, this positioning of the subarrays also covers the horizontal edges of the FOV of the receiver (see the positioning of the time-gating of columns L and R of the array in the xz and yz views in Fig. 26 (c)), which makes it possible to detect a target coming into the FOV of the system from the direction x.

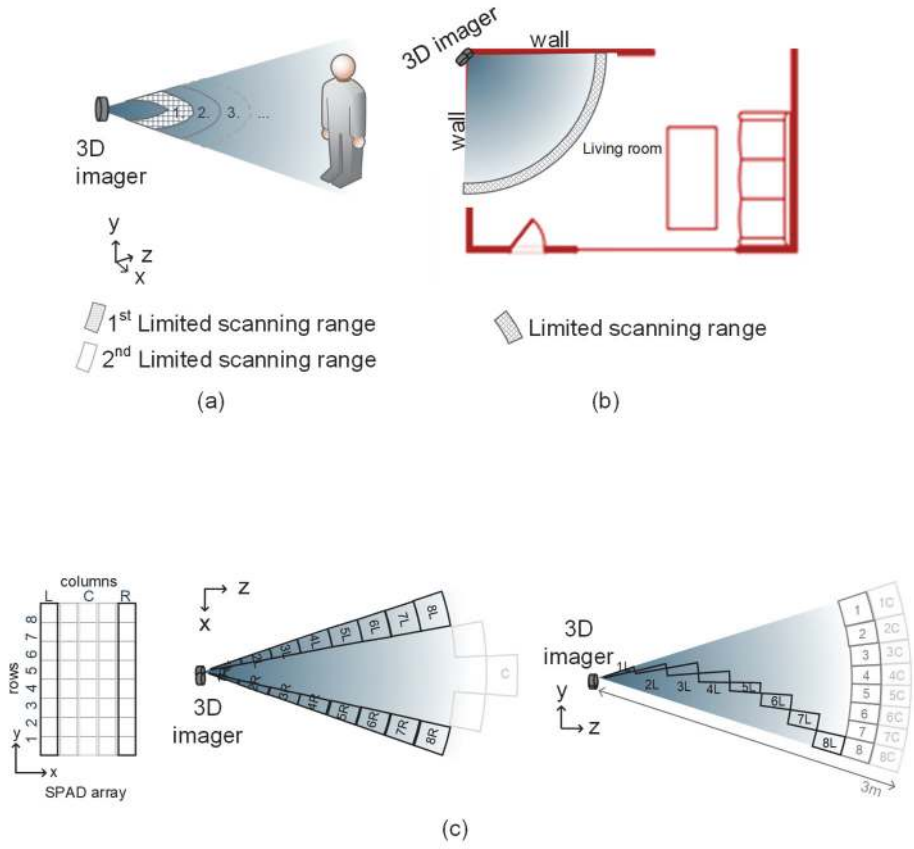

Fig. 26. (a) Positioning of the subarrays at the beginning of an operation. Examples of optimal positioning of the limited scanning ranges (b) when waiting for a new target at a known distance, and (c) depending on the application.

The digital design is implemented on an Arria V FPGA Starter board when using Mathworks Matlab with Simulink for setting the system up and collecting the measurement results. The main components of the receiver PCB are shown in Fig. 27. A latency of 72 ns (6 cycles of a 83 MHz clock) for determining the distance after the last pulse has been measured and a latency of ~1 µs (84 cycles) for determining the next scanning range have been achieved.

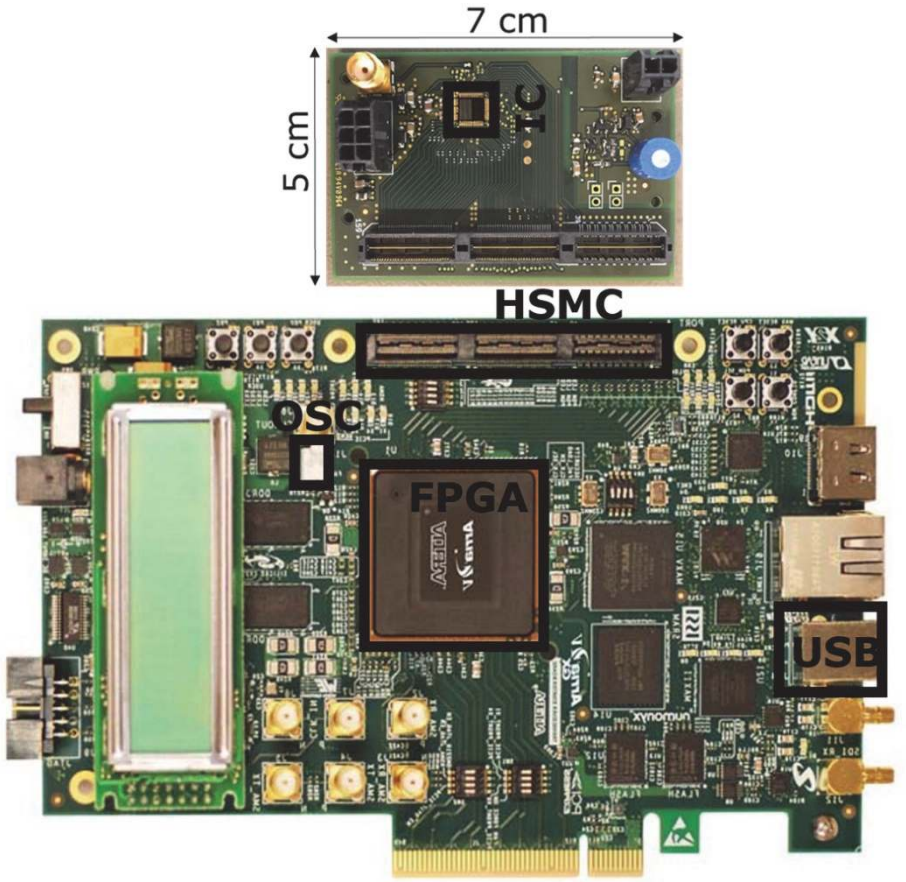

Fig. 27. Main components of the receiver: IC, HSMC connector, Arria V FPGA, oscillator and USB connection. An FPGA Arria V starter board is used for fast prototyping.

5 3D imaging results

During this work the imaging system first had a larger FOV (36° × 57°), yielding the corresponding results reported in paper II. The FOV of the receiver optics was then reduced so that it was possible to measure longer distances with low (~0.1 mW) average optical power of the laser source. The results obtained with that system and a FOV of 18° × 28° are presented in Paper III, and the main results are also summarized in this chapter.

In the course of the work, however, the laser source was improved so that the pulsing rate and optical power could both be increased relative to the values used in Papers II and III. The first imaging results obtained with the new laser source are presented in Paper IV, where a laser pulsing rate of 700 kHz, an FWHM of 200 ps and an average optical power of 4.7 mW were used. By the end of the experimentation the pulsing rate had been increased to 926 kHz and the corresponding new measurements, which demonstrate the effect of the resulting increase in the frame rate, are presented in this chapter.

Active illumination of the measurement scene (system FOV) was produced with one laser diode, the pulse from which was spread over the field-of-view of the receiver with a diffuser. The non-homogeneity of the illumination, together with the variation in photon detection probability among the SPADs of the array will affect the number of signal photons detected in the various pixels, and can even be seen in a lack of signal detections in the corner pixels of the array in the distance results if the averaging factor is too low. To demonstrate this, an example will be presented next of the measurement of signal detections in the array when the laser pulse is reflected from a white paper target located perpendicular to the optical axis of the imager system.

5.1 Illumination homogeneity

In the optimum case the laser pulse energy should be spread homogeneously over the FOV of the receiver and no signal energy should be wasted outside the FOV. The present approach, in which the laser pulse is spread using a diffuser, is a simple and cheap solution, but the illumination achieved is concentrated more on the central part of the array and the borders receiver less photons, which may lead to a lack of signal results in the pixels on the border if the number of laser pulses measured is too low. The photon detections were measured using a white paper target placed on the wall 3.55 m away from the imager to study the non-

homogeneity of the illumination, and it turned out that the probability of photon detections was higher when part of the array was not operating or if the time-gating positions in some of the sub-arrays were further away from the sub-array under consideration. The reason why the probability of photon detection decreases when all the time-gating signals are located in the same position is most probably connected with a drop in the power supply voltage, and this should be taken into account when determining the strategy for positioning the time-gating signals. Normalized photon detection maps for a case in which some of the subarrays were not operating are shown in Fig. 28. The results depict higher energy at the centre of the array, which is mostly due to the inhomogeneity of the illumination, although the results also include the effect of the non-uniformity of the photon detection efficiency of the array which results from variations in the SPAD characteristics and can be seen as a crumbled surface in a 3D representation, see Fig. 29, which shows pixel rows 20-40 of Fig. 28 (b) and pixel rows 1-20 of Fig. 28 (c).

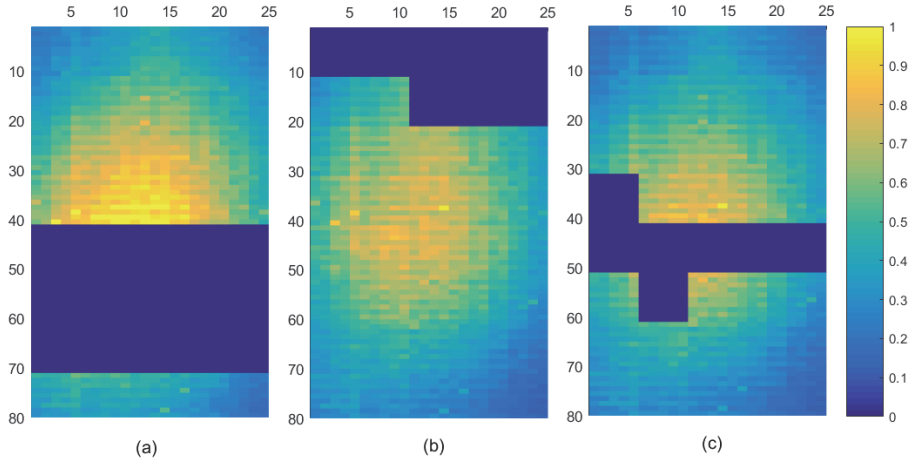

Fig. 28. Normalized photon detections when some of the subarrays are not operating.

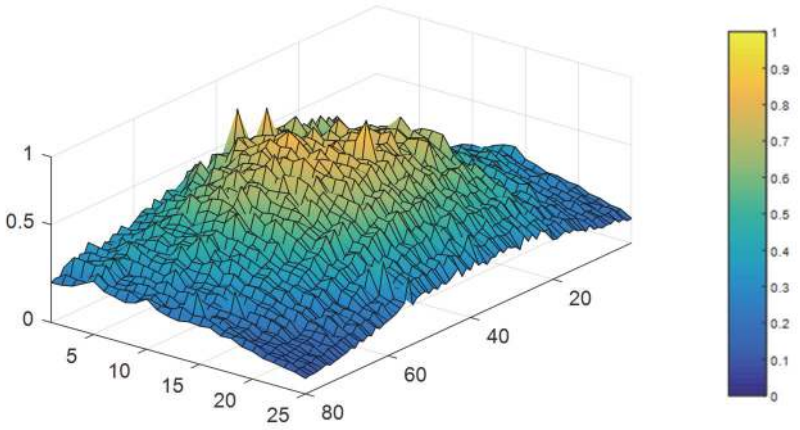

Fig. 29. Normalized signal photon detections showing the illumination non-homogeneity combined with sensitivity differences among the pixels (pixel rows 20-40 are from Fig. 28 (b) and pixel rows 1-20 are from Fig. 28 (c)).

5.2 Distance results

To demonstrate the functionality of the system and the effect of limiting the scanning range around the surfaces seen by the subarrays, the distances of the surface points and the intensities of the photon detections were measured from a scene in which a folder was placed on top of a drawer located in front of a wall. A picture of the scene taken with a high-resolution RGB camera is shown in Fig. 30 (a), and the normalized photon detection rates and distance results for the 25 × 80 pixels are shown in Fig. 30 (b) and (c). A point cloud representation of the results when the FOV of the imager was scanned in the z direction starting from the first target up to the back wall is shown in Fig. 31 (a), and the result obtained when the scanning was limited around the surfaces seen in the FOV of each subarray is shown in Fig. 31 (b). In these measurements, the frame rate increased by a factor of 13 from 0.7 frames per second (fps) to 9 fps when the scanning range was limited from 2.7 m in Fig. 31 (a) to 21 cm in Fig. 31 (b). A precision of $\sigma \leqslant 1.6$ cm was measured for the drawer and $\sigma \leqslant 2.1$ cm for the back wall and the folder in Fig. 31 (b). More results are presented in Paper III.

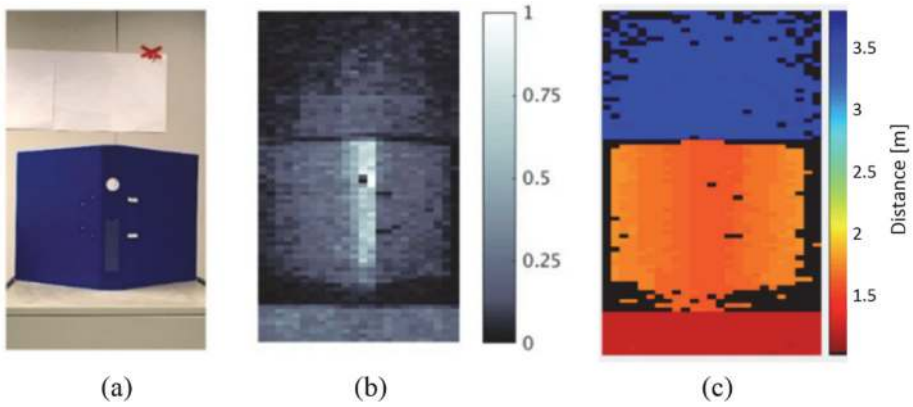

Fig. 30. (a) Picture of the scene (b), normalized photon detection rates (c) and the distance result obtained from 25 x 80 pixels (Reprinted by permission from Paper III © 2019 IEEE).

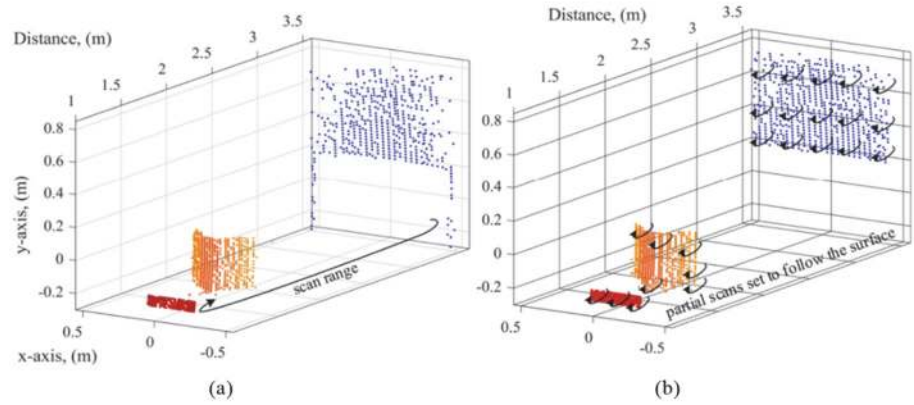

Fig. 31. Point cloud representation of (a) scanning the full range (b), limiting the scanning range to 21 cm around the surfaces (Reprinted by permission from Paper III © 2019 IEEE).

The custom-made laser diode source in the above measurements had a wavelength of 864 nm, a pulsing rate of 100 kHz, FWHM ~110 ps, and the energy of a pulse was ~1 nJ (Kostamovaara et al., 2015). The laser source was then changed to another custom-made bulk laser diode which had a wavelength λ of 882 nm, FWHM of 200 ps, linewidth of ~5 nm, pulse energy of >6 nJ and maximum pulsing rate of 1 MHz (Huikari, Avrutin, Ryvkin, & Kostamovaara, 2016). In all the

measurements a 50 nm bandpass filter having a centre wavelength of 875 nm was used in front of the receiver.

The increase in frame rate achieved with the modified laser transmitter is demonstrated with measurements from a scene in which a gym ball was located in front of a wall that was covered with white paper, see the picture of the scene in Fig. 32 (a). The distances from the surfaces in the FOV of the receiver were measured by scanning the range with time-gate steps of 202 ps and applying 30 cm partial scanning ranges around the first target surface detected in the FOV of each subarray. The time-gate positions which had the maximum photon detections were used to calculate the distance, and normalized photon detections in that time-gate position are shown in Fig. 32 (b). In this range scan, 1920 laser pulses were sent for each time-gate position. In the intensity result shown in Fig. 32 (c) two partial scanning ranges of 30 cm were measured for each subarray. The colour difference that can be seen around the ball in pixel rows 30-80 in Fig. 32 (c) compared with Fig. 32 (b) is due to two partial scanning ranges. When another partial scanning range was added, the echo of the laser pulse could also be detected in those pixels for which the wall was in the FOV, even though the first partial scanning range of the subarray was set around the surface of the ball. The benefit of a second partial scan is more evident in the range image results shown next.

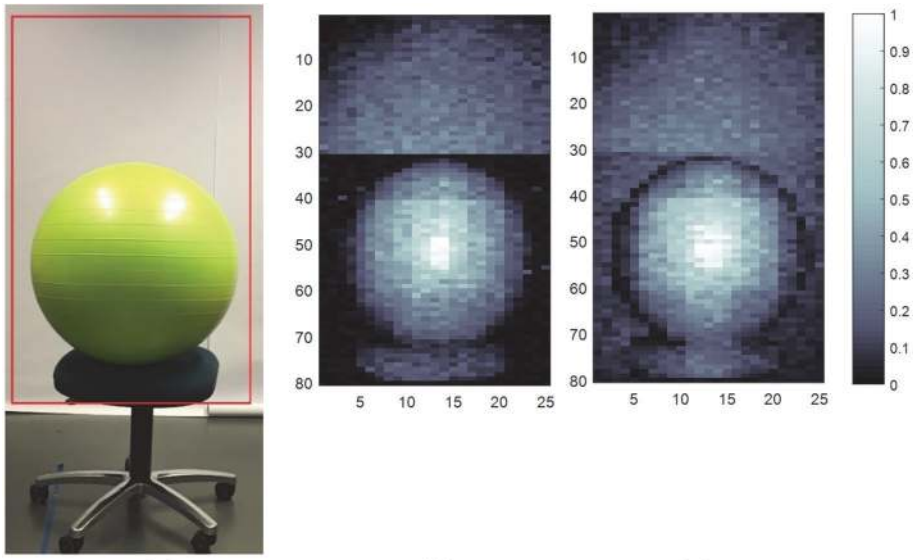

Fig. 32. (a) Picture of the scene. (b) Normalized photon detections in the SPAD array when 30 cm partial scanning ranges are defined around the first target surface detected in the FOV of each subarray (1920 laser pulses sent for each time-gate position), (c) second partial scanning range added around the second surface.

3D range imaging results obtained when limiting the scanning range to 30 cm around the first surface in the FOV of the subarrays are demonstrated in Fig. 33 (a). The limiting of the scanning range to around the nearest surface in the FOVs of the subarrays can be seen from the lack of blue points (around the ball) in Fig. 33 (a) compared with Fig. 33 (c), in which a second partial scan is added around the second surface. Obviously, if one partial scanning range is used the frame rate is doubled compared with implementing two partial scanning ranges for each subarray.

The frame rate can also be increased by reducing the number of laser pulses measured per time-gate position, see Fig. 33 (b) and (d), in which 960 laser pulses were sent for each time-gate position as compared with Fig. 33 (a) and (c), which were based on 1600 laser pulses. Reducing the number of laser pulses will increase the frame rate by the same factor. However, the decreased numbers of sent laser pulses for each time-gate position result in Fig. 33 (b) and (d) seem to be located in noisier pixels and even lack of distance result, especially in the boundary region of the ball in which the echo signal arriving at the receiver is low.

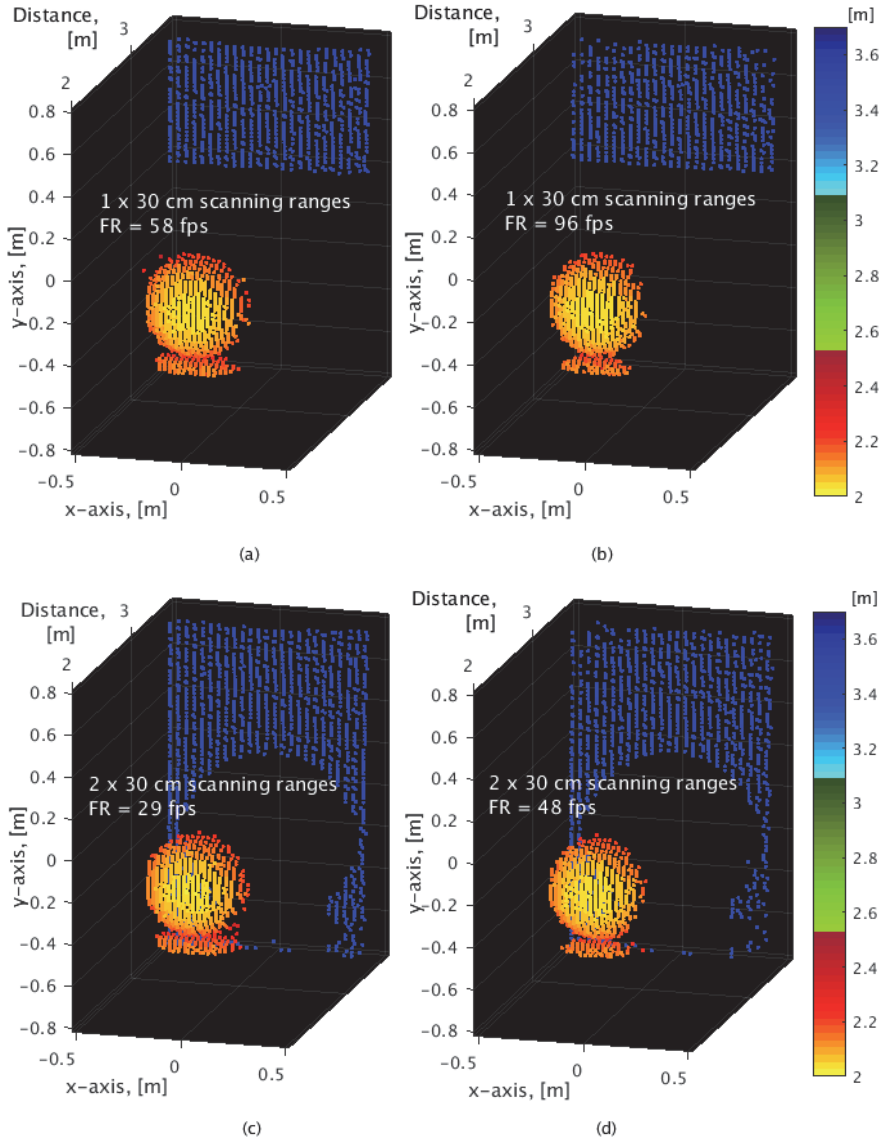

Fig. 33. Demonstration of the point clouds with one or two partial scanning ranges of 30 cm. The number of laser pulses sent for each time-gate position is (a) 1600 (1 range, FR=58 fps), (b) 960 (1 range, FR=96 fps), (c) 1600 (2 ranges, FR=29 fps) (d) 960 (2 ranges, FR=48 fps).

5.3 Noise tolerance of the system

As explained above, this 3D range imaging system has a topology in which the SPADs are activated for only a short period at a time. If a SPAD is activated at the moment when the echo signal arrives at the detector, the probability of the SPAD being triggered due to ambient light and blocking the echo signal is low. This inherent tolerance of the system with respect to ambient light was tested by illuminating the test surface (a wall at 3.5 m) with a halogen lamp. A picture of the scene taken with a high resolution RGB camera when the halogen lamp was illuminating the wall is shown in Fig. 34 (a). The photon detections of the scene under low ambient lighting conditions (office lighting) were measured with the SPAD array when neither the laser nor the halogen lamp was operating, see Fig. 34 (b), where 1600 samples were taken and the time-gate was set to the minimum (0.8 ns). The result shows that the number of photon detections is low, since it is dependent on the relatively low DCR of the sensor itself and the low lighting conditions. The ambient light was then increased by turning the halogen lamp on and new photon detections were measured, see the result obtained from 1600 samples in Fig. 34 (c), where the increased ambient light has led to an increased number of photon detections in those pixels that see the wall, especially between the lamps. After the laser was turned on, the scene was scanned by delaying the time-gate in 202-ps steps and counting the triggerings of the SPADs from 1600 laser pulses for each step. The number of photon detections in the time bin gathering the maximum of hits within the scan is shown in Fig. 34 (d). The increased number of photon detections due to active illumination by means of the laser can be seen by comparing Fig. 34 (c) and (d) e.g. from the backs of the lamps.

Fig. 35 (b) shows a few histograms from a pixel located at the centre of the array (column 13, row 40) under increased ambient lighting conditions (as in Fig. 34 (d)), while the results for the same pixel in office lighting are shown in Fig. 35 (a). As can be seen from Fig. 35, the number of average photon detections in the central pixel increases by a factor of ~30 in (b) and ~120 in (c) due to the increased ambient light, but the echo signal (peak above the noise floor) remains at about the same level and thus can still be detected. However, multiple measurements needs to be averaged for the signal to be detected from the noise in high ambient lighting conditions.

Correspondingly, Fig. 36 (a) shows a range image of the scene when 1600 laser pulses were sent for each time-gate position in office lighting and Fig. 36 (b) shows the result when the ambient light was increased to irradiance of up to

8 µW/(cm^2·nm) (measured at the center of the target surface). The noise arising from the added lighting resulted in false detections in some of the pixels in the latter case, but the effect of noise can be attenuated by increasing the number of laser pulses for each time-gate step, see the result in Fig. 36 (c), in which the number of laser pulses for each time-gate position was doubled to 3200. The scene was first scanned through after which two partial scanning ranges of 30 cm were fixed around the target surfaces. The laser pulsing rate was 926 kHz resulting frame rate of 29 fps for Fig. 36 (a) and (b) and 14 fps for Fig. 36 (c). The max standard deviation of the measured distance results in the central pixels (x=35 to 45, y=11 to 14) was reduced from 7 cm to 1.3 cm from Fig 36 (b) to (c).

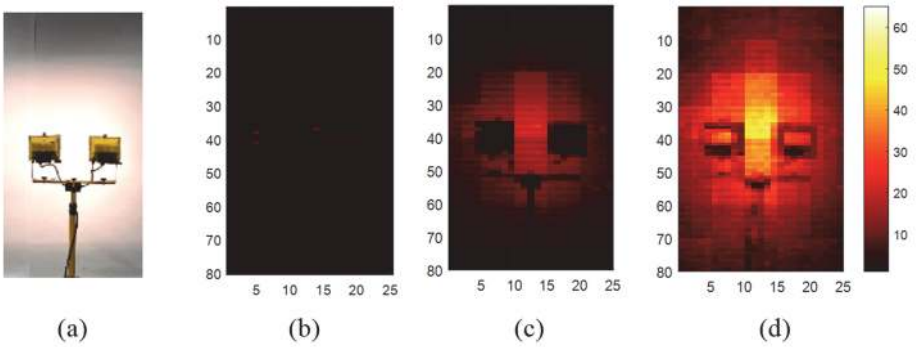

Fig. 34. (a) Picture of the scene taken with a high resolution RGB camera. Numbers of photon detections when the laser is not operating and 1600 samples are taken for each time-gate position (b) in office lighting and (c) when the ambient light is increased by turning the halogen lamps on. (d) Number of photon detections with the laser on.

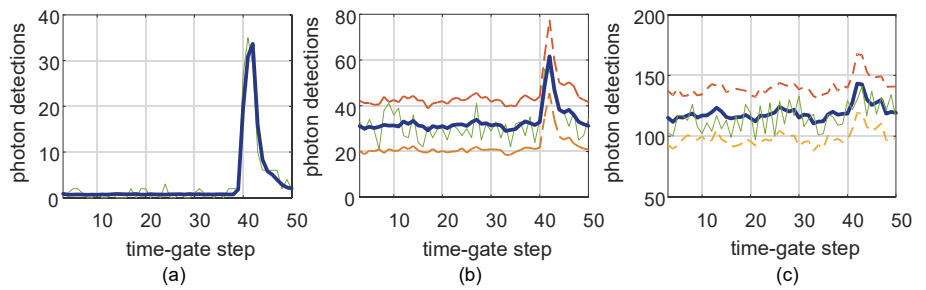

Fig. 35. Histograms of a central pixel (column 13, row 40) (a) in office lighting, (b) with the ambient lighting at the target increased to 8 µW/(cm^2·nm) and (c) to 34 µW/(cm^2·nm). One measured histogram and an average result of 100 histograms (bold) are shown in panels (a), (b) and (c). Also ±2 standard deviations are indicated by dotted lines.

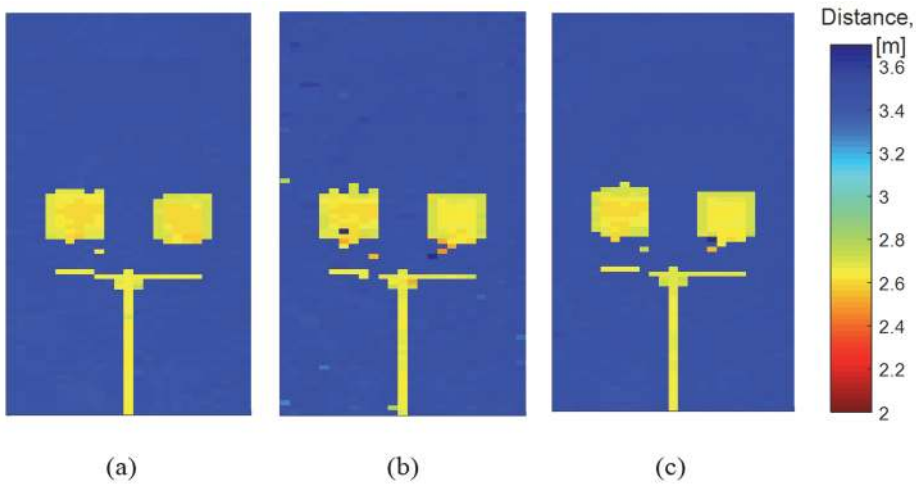

Fig. 36. Distance results from the pixels when 1600 laser pulses are sent for each time-gate position (a) in office lighting and (b) at maximum irradiance of 8 µW/(cm²·nm) measured from the centre of the target surface, and (c) when the number of laser pulses is increased to 3200 for each time-gate position.

In order to characterize the quantitative effect of the halogen lamps on the background illumination, measurements were carried out with a lux meter (Voltcraft BL-10L). This showed a maximum of 1.3 klux (±10%) at the wall between the halogen lamps, but since it filters out any irradiance that lies beyond the wavelengths of visible light (where halogen lamps have their maximum power), the effect of the additional light from the halogen lamps at the receiver was also measured with another optical power meter with its optical input signal filtered with the same optical bandpass filter that was used in front of the SPAD array, in order to measure the irradiance seen by the SPAD array. The maximum measured irradiance of the light at the target surface was 8 µW/(cm²·nm) (±20%), which is comparable to the daylight illuminance of ~10 klux with a bandpass wavelength of 875 nm (Stoffel et al., 2010).

5.4 Frame rate of the system

The frame rate of the system depends on the number of scanning steps (depth of the scanning, i.e. range of interest), the pulsing rate of the laser source (at a given pulse energy), the reflectivity of the target and the ambient light. The latter two parameters may increase the averaging factor needed and thereby reduce the frame

rate. To limit the scanning range effectively around the surface of a fast-moving target, not only does the frame rate of the distance measurement have to be fast enough but also the sliding of the limited scanning range has to keep pace with the movement of the target.

A demonstration of the speed of the algorithm implemented on the FPGA is provided in Fig. 37, which shows that the partial scanning ranges of subarrays around a ball can shift from ~3.5 m (back wall) to ~1 m (ball surface) quickly enough when a target is located in the adjacent pixels of the nearest subarray so that the range imager is able to follow the X-Y movement of a dropped ball.

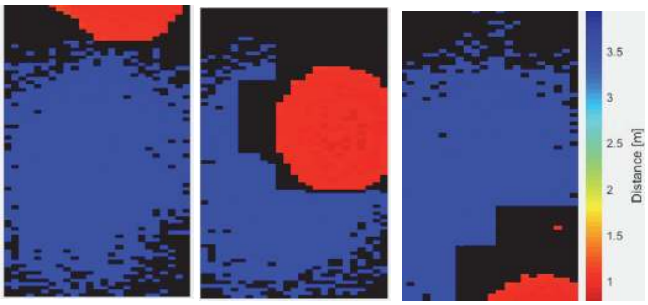

Fig. 37. Demonstration of the effect of shifting the limited range scan of the subarrays from the back wall at 3.5 m to the front when a ball has been dropped at a distance of 1 m. The scanning range was set to 30 cm and the frame rate of the measurement was 70 fps (Reprinted by permission from Paper IV © 2019 Society for Imaging Science and Technology).

The partial scanning range follows the echo signal in the time domain, which makes it possible to follow a target with a limited scanning range in the direction z when the target moves towards the imager system or further away from it. If the frame rate is set at 70 fps, the partial scanning range at 30 cm and the next partial scanning range is positioned so that the detected echo signal is in the middle, it should be possible to follow a target moving at a speed of ~10 m/s (0.15 m·70 fps). This capability of the system is demonstrated in Fig. 38, which shows 5 frames of the X-Y point clouds of a moving ball (kept at the end of a rope, see the image of the hand in frame 3) taken at a time interval of ~132 ms. The frame rate of the measurement was 70 fps and the partial scanning range was set at one sub-range of 30 cm with a 3-cm scanning step. In this example the positions of the partial scanning ranges of the subarrays change from one frame to another depending on the position of the target, which moves in the directions y and z.

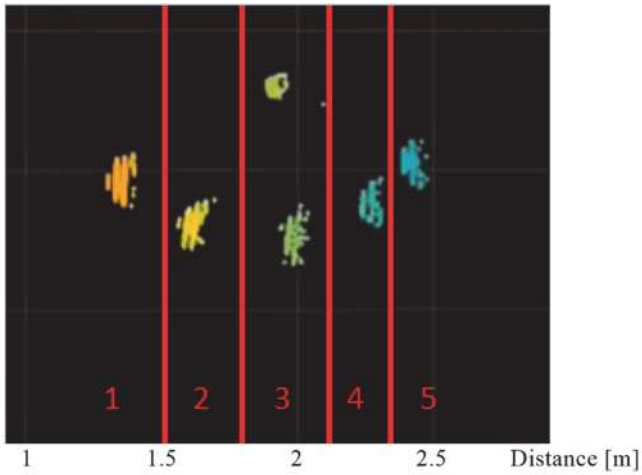

Fig. 38. Combined Y-Z point cloud snapshots of distance measurement of a ball moving away from the imager. The time interval between the snapshots is ~132 ms (frame rate 70 fps).

6 Discussion

It is proposed here that the frame rate of the sliding time-gate technique used to measure the time-of-flight of a short laser pulse can be increased by limiting the scanning range around the target surfaces. In addition, the adaption of the system's FOV to varying target scenarios can be improved by dividing the array into independently controllable subarrays. A 3D range imager prototype has been developed that is able to limit the unit scanning of a range of 3.3 m to partial scanning ranges of 21 cm, which increases the frame rate by a factor of 16. On the other hand, independently controlled subarrays increase the complexity of the controller, since the next partial scanning range for each of the subarrays has to be determined separately before the next measurement is made.

The amount of in-pixel electronics needed for an image sensor using the above-mentioned technique is fairly low, which makes it possible to realize large pixel arrays with a good fill factor. Also, the data collected from the sensor after each laser shot is just 1-bit detection/no-detection information about the corresponding histogram bin, which results in a low data rate. This in turn means that the laser pulsing rate in the prototype can be increased to ~1 MHz. One very important point is that the peak of the histogram can be detected simultaneously as the scan proceeds, since the histogram bins are measured one at a time. For this reason it is not necessary to save the full histograms for each pixel, as is usually necessary in TDC-based systems.

A comparison with other relevant optical solid-state 3D range imaging sensors is presented in Table 1. Numerous improvements have been made to 3D range imager systems while this PhD research has been going on, and the trend has been towards more advanced technology nodes and even 3D BSI stacked technologies, which allows smaller pixel pitches and larger arrays. In conclusion, the achievable 3D image frame rate of the imager developed in this work is high with respect to the illumination level and power consumption, even though the realization took place in the conservative CMOS 0.35 μm technology node. The fill factor of the SPAD array is also relatively high, even without the use of micro-lenses. The highest number of pixels can be found in the work of (Bamji et al., 2015), but these are non-SPAD pixels, and the fill factor is also the best, due to the optimally designed micro-lens array implemented on top of the pixel array. The mm-level precision is achievable with direct TOF imagers even at the range of 50 m (Zhang et al. 2019), however, the precision at the measurement speed of 30 fps is not reported. Usually solid state direct TOF imagers are used in dark as in (Zhang et al.

2019) but methods for tolerating ambient lighting and maintain reasonable frame rate are being in the research interest of multiple research groups. The frame rate of 30 fps has been achieved in ambient lighting of 1 klux at the range of 50 m in (Henderson, Johnston, Hutchings et al., 2019) by combining multiple SPADs in one pixel and using coincidence detection and implementing the SPAD array with 90 nm BSI technology connected with hybrid bonding to timing circuitry implemented with 40 nm technology. Techniques to tolerate high ambient lighting have been studied also with non-SPAD sensors and usually high optical power is needed. In (Hsu et al. 2018) precision of 4.2% of the range have been reported with 26 fps with very bright ambient lighting of 180 klux, however optical power > 2 W is needed together with narrow FOV.

Table 1. Recently published solid-state optical 3D range imagers

Reference	Bamji et al. 2015	Hsu et al. 2018	Zhang et al. 2019	Henderson, Johnston, Hutchings et al. 2019	Niclass et al. 2008	This work		
ToF tech.	cw-iTOF	pl-iTOF	direct TOF	direct TOF	direct TOF	gate scan		
ToF pixels	512 × 424	64 × 64	252 × 144	64 × 64	128×128	25 × 80		
Pixel type	polygates	photo-	SPADs	SPADs	SPADs	SPADs		
(total pixels)		diodes		(256×256)				
CMOS Technology	0.13 µm	0.18 µm	0.18 µm	40/90 nm BSI	0.35 µm HV	0.35 µm HV		
Fill Factor	60%(1)	33%	28%	51%	6%	32%		
FOV	70°×60°	2.9°×2.9°	40°×20°	1.2°×1.2°	5°	18°×28°		
Operating mode						High perf.(6)	High speed(7)	Low power(8)
Optical power	600 mW	2.6 W	2 mW	1.8 mW	1 mW	6.2 mW	4.7 mW	0.1 mW
Wavelength	860 nm	850 nm	637 nm	671 nm	635 nm	882 nm	882 nm	864 nm
Mean power(2)	2.1 W	not stated	2.54 W	78 mW	not stated	521 mW	386 mW	59 mW
(timing circuitry)						(83 mW)	(56 mW)	(10 mW)
Measured range with	3.5 m	7.5 m	0.7 m	50 m	3.75 m	3.5 m	3.5 m	3.5 m
ambient light,	3 klux	180 klux	dark	1 klux	150 lux	10 klux	200 lux	200 lux
reflectivity,	10%	not stated	white	white	not stated	white	white	white
3D image FR,	30 fps	26 fps	30 fps(4)	30 fps	-(3)	14 fps	70 fps	9 fps
precision (σ)	1.5 cm	4.2%	-(5)	not stated	0.5 cm	1.3 cm	1.5 cm	2 cm

(1) with microlenses

(2) average power consumption of the sensor array IC

(3) 50 ms acquisition time reported, however, final 3D image frame rate not reported

(4) only half the array was measured and median filter of 2 x 2 used for the result lowering the spatial resolution of the image to 63 x 72 pixels

(5) precision σ =1.4 mm was reported up to 50 m with 30 000 photons collected into a histogram, precision for 3D image frame rate of 30 fps not stated

(6) laser pulsing rate fpulse= 926 kHz, PSR = 2 x 30 cm

(7) fpulse= 700 kHz, PSR = 30 cm (Paper IV)

(8) fpulse= 100 kHz, PSR = 21 cm (Paper III)

One special feature of this work is that the realization described here can be used with a miniaturized custom-made laser diode-based illuminator that uses high-energy (~1…7 nJ) and high-speed (~150 ps) pulses for the TOF measurements. This approach, in combination with the proposed receiver system architecture and realization, results in high measurement precision and high immunity from background illumination, as is demonstrated in the measurements presented above.

There are some improvements that could be made to the imager sensor developed in this work even in the same HV 0.35 μm technology node. The layout has been designed so that the total area can be easily multiplied by four simply by copying the layout four times. The drawback of the increased receiver area would be increased power consumption of the sensor. Also, the optical illumination power should be increased accordingly to keep the signal power the same for each pixel. In addition, the data readout rate from the chip would decrease by a factor of two due to pipelining of the readout registers.

The INL of the on-chip DLL could be improved by reducing simultaneous digital events and redesigning the power supply distribution. For some applications it could be beneficial to completely remove the DLL2 and double the length of the DLL1. This solution would give ~200 ps timing steps and a range of 48 ns, which would correspond to a measurement range of around 7.2 m. An additional timing-grid improvement could be made with an adjustable delay for the laser output triggering signal of 50 ps or 100 ps, for example.

The FPGA design could be improved by adding an automatic noise level detection and signal threshold definition for each pixel separately. The threshold levels could be calculated depending on the noise levels in the partial histograms. The threshold used in the measurements in this work was the same for all the pixels in the array, leading to problems in limiting the scanning range when some pixels have high noise due to ambient lighting, for example, while others have low noise, as in the scene in Fig. 34 (a). When some pixels have a high noise level due to ambient light, a high threshold has to be set for the signal, which leads to a lack of signal detection in those pixels which have lower ambient light levels if only one threshold level has been implemented for the whole array.

The results were achieved in fairly conservative technology, with a gate density of 23 kgates/mm^2 and only 4 metal layers. The improvements mentioned above would presumably be significant when transferring the design into technology nodes that permit higher gate densities and greater numbers of metal layers, even if the performance of the SPADs were to remain more or less the same. The fill factor of the sensor would increase if the in-pixel digital solution had a higher gate

density, so that a fill factor of around 50% has been estimated for an array of 160 x 100 pixels (each with an area of 50 µm x 50 µm) with 25 pixels per subarray when transferring the design from a 0.35 µm to a 0.11 µm technology in which the gate density is 13 times higher. This calculation assumes that the SPADs can be placed 40% closer to each other, that one additional metal layer can be reserved for routing and that the electronics can be scaled directly. The readout speed from the sensor part of the chip could be increased to match the laser pulsing rate (e.g. 1 MHz) even with an increased number of pixels by employing faster digital logic. The increased gate density would also make it beneficial to implement more signal processing on the sensor chip, which would reduce the power consumption as a result of lower I/O data rate to the FPGA.

The fill factor of the current design could be increased by implementing micro-lenses, and adopting a BSI 3D stacked hybrid structure for the technology would raise the fill factor even more and also increase the amount of in-pixel electronics without detracting from the fill factor. An in-pixel TDC with a resolution of 4 bits inside each time-gate would increase the frame rate 16-fold compared with the scanning of 16 time-gate positions in successive measurements. The improvement in speed would nevertheless only be valid when the fill factor remains the same (which is presumably possible only with a BSI 3D stacked structure).

Depth images are usually converted to point-cloud representations, which often results in sparse images due to low resolution, and also a lack of distance in some of the pixels due to low illumination power combined with low target reflectivity, for example. These sparse and often also noisy point-clouds from the 3D range imager can be enhanced using advanced image processing methods (Altmann et al., 2018), e.g. spatial correlations between photons (Kirmani et al., 2014), deep learning (Niu et al., 2018) or data fusion with a RGB camera (Chan et al., 2019). However, the use of such methods to improve the quality of the depth results may be considered to lie beyond the scope of the present work.

7 Summary

Solid-state light detection and ranging (LiDAR) is one of the most promising sensor technologies for applications that need a low cost, small-sized, high performance range imager for use in a three-dimensional space (3D), such as gesture control, augmented or virtual reality (AR/VR), advanced driver-assistance systems (ADAS) and autonomous driving.

Time-of-flight (TOF) techniques using continuous wave laser illumination are widely used for 3D depth imaging in consumer products at the moment, achieving large pixel arrays (up to 1 Mpixels). They nevertheless involve a trade-off between an unambiguous range and the precision of the measurement which typically limits their usage to ranges of 6 m or less. In direct TOF techniques the time-of-flight is measured directly from the delay in the echo of a laser pulse, and the maximum range depends in principle only on the signal energy, i.e. the optical power of the laser. To achieve single photon sensitivity in the sensor with a cost-effective solution, a single photon avalanche diode (SPAD) array implemented in standard complementary metal oxide semiconductor (CMOS) technology can be used.

Direct TOF imagers employing a time-to-digital converter for each SPAD in the array have achieved high performance with low active optical power under dark ambient lighting conditions, but when the ambient lighting is increased the SPADs may be triggered by noise before the echo signal from the laser pulse arrives at the sensor, thus lowering the probability of the echo signal being detected. Another limiting factor is the large amount of data to be transferred from the pixel array to the post-processing stage. An array of 2 kpixels with an 8-bit distance result for each laser pulse at a pulsing rate of 1 MHz would result in an I/O data rate of 16 Gbit/s, for example. Several techniques have been proposed for lowering the I/O data rate but this factor still limits the speed of the measurement in large arrays.

This thesis has been concerned with the development of a solid-state time-of-flight 3D range imager technique in which the echo of a short laser pulse is detected by sliding the time-gate (<0.8 ns) of a SPAD array in small steps over successive measurements. The length of the time-gate was minimized in order to reduce the effect of noise that is partly intrinsic to the sensor (dark counts) but mostly arises from ambient light. The timing information on the photons that are able to trigger the SPADs is stored in the FPGA controller, which leads to a much lower rate of data passage from the sensor than is needed in a TDC based system. Similarly the memory resources needed for the post-processing can be highly compressed due to the already known timing of photon detection (the time gating approach).

An illumination scheme that is based on short, intensive laser pulses can pave the way for increasing the frame rate of 3D range imaging, since the measurement range can be limited to an area around the surface of the target. For high flexibility in terms of target scenarios, the SPAD array was divided here into 40 subarrays. This means that the scanning ranges of the subarrays can be defined more effectively, which speeds up the frame rate considerably. For example, by limiting the scanning of a 3.3 m range to a distance of only 21 cm around the target surfaces increases the frame rate by a factor of 16. The drawback of dividing the array into subarrays is the need for additional electronics on the sensor chip and routing to control the time-gating of the 40 subarrays as opposed to only one time gate for the whole array. The additional electronics are digital in nature, however, and can be scaled down when transferring the design to a more advanced technology node. Also, controlling the subarrays separately increases the processing power needed, since the shifting of the partial scanning ranges has to be decided for each subarray depending on the target range and its movements.

The solid-state 3D range imager prototype system using short laser pulses (~200 ps) and time-gating of a SPAD array that was developed and realized following the above design principles has 2000 pixels, each of which has one SPAD and only small amount of electronics, resulting in a high fill factor of 32% even when implemented in a fairly conservative 0.35 μm technology. The frame rate of the 3D range image depends on the scanning steps, the laser pulsing rate and the number of laser pulses needed for each time-gate position, which is related to the laser pulse energy, target reflectivity and noise. An FPGA-based algorithm was also developed for setting the time-gate positions depending on the range of target surfaces, and 3D range imaging results were obtained up to a distance of ~4 m at a speed of 9 frames per second with an average optical power of 0.1 mW by limiting the scanning range around the surfaces of the targets with 200 ps delay steps, resulting in ~3 cm depth resolution. The frame rate could be increased to ~70 fps by raising the laser pulsing rate and average optical power to 700 kHz and ~5 mW, respectively. The tolerance of background lighting was also measured, with the results showing a precision of a few cm at a range of 3.5 m in ambient lighting conditions corresponding maximum of ~10 klux daylight when the frame rate was set at 14 fps. This demonstrates that the time gating technique used in this work prevents the sensor from saturating and enables the imager to be used even under bright ambient lighting conditions.

List of references

Abbas, T. A., Dutton, N. A. W., Almer, O., Pellegrini, S., Henrion, Y., & Henderson, R. K. (2016). Backside illuminated SPAD image sensor with 7.83µm pitch in 3D-stacked CMOS technology. Paper presented at the *2016 IEEE International Electron Devices Meeting (IEDM),* 8.1.-8.1.4. doi:10.1109/IEDM.2016.7838372

Altmann, Y., McLaughlin, S., Padgett, M. J., Goyal, V. K., Hero, A. O., & Faccio, D. (2018). Quantum-inspired computational imaging. *Science, 361*(6403), eaat2298. doi:10.1126/science.aat2298

Andersson, P. (2006). Long-range three-dimensional imaging using range-gated laser radar images. *Optical Engineering, 45*(3), 034301.

Bamji, C. S., O'Connor, P., Elkhatib, T., Mehta, S., Thompson, B., Prather, L. A., . . . Chan, V. (2015). A 0.13 µm CMOS system-on-chip for a 512 × 424 time-of-flight image sensor with multi-frequency photo-demodulation up to 130 MHz and 2 GS/s ADC. *IEEE Journal of Solid-State Circuits, 50*(1), 303-319. doi:10.1109/JSSC.2014.2364270

Bamji, C. S., Mehta, S., Thompson, B., Elkhatib, T., Wurster, S., Akkaya, O., . . . P. O'Connor. (2018). IMpixel 65nm BSI 320MHz demodulated TOF image sensor with 3µm global shutter pixels and analog binning. Paper presented at the *2018 IEEE International Solid - State Circuits Conference - (ISSCC),* 94-96. doi:10.1109/ISSCC.2018.8310200

Beer, M., Haase, F. J., Ruskowski, J., & Kokozinski, R. (2018). Background light rejection in SPAD-based LiDAR sensors by adaptive photon coincidence detection. *Sensors, 18*(12), 4338. doi:10.3390/s18124338

Bellisai, S., Bronzi, D., Villa, F. A., Tisa, S., Tosi, A., & Zappa, F. (2013). Single-photon pulsed-light indirect time-of-flight 3D ranging. *Optics Express, 21*(4), 5086-5098.

Bronzi, D., Zou, Y., Villa, F., Tisa, S., Tosi, A., & Zappa, F. (2016). Automotive three-dimensional vision through a single-photon counting SPAD camera. *IEEE Transactions on Intelligent Transportation Systems, 17*(3), 782-795. doi:10.1109/TITS.2015.2482601

Bruschini, C., Homulle, H., Antolovic, I. M., Burri, S., & Charbon, E. (2019). Single-photon avalanche diode imagers in biophotonics: Review and outlook. *Light: Science & Applications, 8*(1), 87. doi:10.1038/s41377-019-0191-5

Burri, S., Maruyama, Y., Michalet, X., Regazzoni, F., Bruschini, C., & Charbon, E. (2014). Architecture and applications of a high resolution gated SPAD image sensor. *Optics Express, 22*(14), 17573-17589.

Busck, J., & Heiselberg, H. (2004). Gated viewing and high-accuracy three-dimensional laser radar. *Applied Optics, 43*(24), 4705-4710. doi:10.1364/AO.43.004705

Chan, S., Halimi, A., Zhu, F., Gyongy, I., Henderson, R. K., Bowman, R., . . . Leach, J. (2019). Long-range depth imaging using a single-photon detector array and non-local data fusion. *Scientific Reports, 9*(1), 8075. doi:10.1038/s41598-019-44316-x

Charbon, E., Bruschini, C., & Lee, M. (2018). 3D-stacked CMOS SPAD image sensors: Technology and applications. Paper presented at the *2018 25th IEEE International Conference on Electronics, Circuits and Systems (ICECS),* 1-4.

Coates, P. B. (1968). The correction for photonpile-up'in the measurement of radiative lifetimes. *Journal of Physics E: Scientific Instruments, 1*(8), 878.

Dutton, N. A., Parmesan, L., Gnecchi, S., Gyongy, I., Calder, N., Rae, B. R., . . . Henderson, R. K. (2015). Oversampled ITOF imaging techniques using SPAD-based quanta image sensors. In *Proceedings of the International Image Sensor Workshop,* 8-11.

Ficorella, A., Pancheri, L., Dalla Betta, G. -., Brogi, P., Collazuol, G., Marrocchesi, P. S., . . . Savoy-Navarro, A. (2016). Crosstalk mapping in CMOS SPAD arrays. Paper presented at the *2016 46th European Solid-State Device Research Conference (ESSDERC),* 101-104. doi:10.1109/ESSDERC.2016.7599598

Geng, J. (2011). Structured-light 3D surface imaging: A tutorial. *Advances in Optics and Photonics, 3*(2), 128-160.

Ghioni, M., Cova, S., Lacaita, A. & Ripamonti, G. (1988). New silicon epitaxial avalanch diode for single-photon timing at room temperature, *Electron. Lett., 24*(24), 1476-1477, ISSN 0013-5194

Gupta, A., Ingle, A., Velten, A., & Gupta, M. (2019). Photon-flooded single-photon 3D cameras. *Proceedings of the IEEE Conference on Computer Vision and Pattern Recognition,* (pp. 6770-6779).

Haase, J. F., Beer, M., Schrey, O., Ruskowski, J., Brockherde, W., & Vogt, H. (2019). Measurement concept for direct time-of-flight sensors at high ambient light. *Quantum Sensing and Nano Electronics and Photonics XVI. International Society for Optics and Photonics, 10926*, 109260W. doi:10.1117/12.2509779

Harris, C. M., & Selinger, B. K. (1979). Single-photon decay spectroscopy. II. the pile-up problem. *Australian Journal of Chemistry, 32*(10), 2111-2129.

Hecht, J. (2018). Lidar for self-driving cars. *Optics and Photonics News, 29*(1), 26-33.

Henderson, R., Johnston, N., Mattioli Della Rocca, F., Chen, H., Li, D. D. U., Hungerford, G.,. . . Birch, D. J. (2019). A 192 x 128 time correlated SPAD image sensor in 40-nm CMOS technology. *IEEE Journal of Solid-State Circuits,* , 1-10. doi:10.1109/JSSC.2019.2905163

Henderson, R., Johnston, N., Hutchings, S. W., Gyongy, I., Abbas, T. A., Dutton, N., . . . Leach, J. (2019). 5.7 A 256×256 40nm/90nm CMOS 3D-stacked 120dB dynamic-range reconfigurable time-resolved SPAD imager. Paper presented at the *2019 IEEE International Solid- State Circuits Conference - (ISSCC),* 106-108. doi:10.1109/ISSCC.2019.8662355

Hsu, T., Liao, T., Lee, N., & Hsieh, C. (2018). A CMOS time-of-flight depth image sensor with in-pixel background light cancellation and phase shifting readout technique. *IEEE Journal of Solid-State Circuits, 53*(10), 2898-2905. doi:10.1109/JSSC.2018.2850931

Huikari, J., Avrutin, E., Ryvkin, B., & Kostamovaara, J. (2016). High-energy sub-nanosecond optical pulse generation with a semiconductor laser diode for pulsed TOF laser ranging utilizing the single photon detection approach. *Optical Review, 23*(3), 522-528.

Jahromi, S., Jansson, J., & Kostamovaara, J. (2016). Solid-state 3D imaging using a 1nJ/100ps laser diode transmitter and a single photon receiver matrix. *Optics Express, 24*(19), 21619-21632.

Jahromi, S., & Kostamovaara, J. (2018). Timing and probability of crosstalk in a dense CMOS SPAD array in pulsed TOF applications. *Optics Express, 26*(16), 20622-20632. doi:10.1364/OE.26.020622

Kato, Y., Sano, T., Moriyama, Y., Maeda, S., Yamazaki, T., Nose, A., . . . Sukegawa, S. (2018). 320 × 240 back-illuminated 10- μm CAPD pixels for high-speed modulation time-of-flight CMOS image sensor. *IEEE Journal of Solid-State Circuits, 53*(4), 1071-1078. doi:10.1109/JSSC.2018.2789403

Keranen, P., & Kostamovaara, J. (2019). 256x8 SPAD array with 256 column TDCs for a line profiling laser radar. *IEEE Transactions on Circuits and Systems I: Regular Papers,* , 1-12. doi:10.1109/TCSI.2019.2923263

Kirmani, A., Venkatraman, D., Shin, D., Colaço, A., Wong, F. N. C., Shapiro, J. H., & Goyal, V. K. (2014). First-photon imaging. *Science, 343*(6166), 58. doi:10.1126/science.1246775

Kostamovaara, J., Huikari, J., Hallman, L., Nissinen, I., Nissinen, J., Rapakko, H., . . . Ryvkin, B. (2015). On laser ranging based on high-speed/energy laser diode pulses and single-photon detection techniques. *IEEE Photonics Journal, 7*(2), 1-15. doi:10.1109/JPHOT.2015.2402129

Kraft, H., Frey, J., Moeller, T., Albrecht, M., Grothof, M., Schink, B., . . . Buxbaum, B. (2004). 3D-camera of high 3D-frame rate, depth-resolution and background light elimination based on improved PMD (photonic mixer device)-technologies. In *6th Int. Conf. for Opt. Technologies OPTO*, (pp. 95-100).

Lange, R., & Seitz, P. (2001). Solid-state time-of-flight range camera. *IEEE Journal of Quantum Electronics, 37*(3), 390-397. doi:10.1109/3.910448

Lussana, R., Villa, F., Dalla Mora, A., Contini, D., Tosi, A., & Zappa, F. (2015). Enhanced single-photon time-of-flight 3D ranging. *Optics Express, 23*(19), 24962-24973.

Miyagawa, R., & Kanade, T. (1997). CCD-based range-finding sensor. *IEEE Transactions on Electron Devices, 44*(10), 1648-1652. doi:10.1109/16.628817

Morton, G. A. (1949). Photomultipliers for scintillation counting. *RCA Rev., 10*

Mukhtar, A., Xia, L., & Tang, T. B. (2015). Vehicle detection techniques for collision avoidance systems: A review. *IEEE Transactions on Intelligent Transportation Systems, 16*(5), 2318-2338. doi:10.1109/TITS.2015.2409109

Niclass, C., Favi, C., Kluter, T., Gersbach, M., & Charbon, E. (2008). A 128 × 128 single-photon image sensor with column-level 10-bit time-to-digital converter array. *IEEE Journal of Solid-State Circuits, 43*(12), 2977-2989. doi:10.1109/JSSC.2008.2006445

Niclass, C., Soga, M., Matsubara, H., Kato, S., & Kagami, M. (2013). A 100-m range 10-frame/s 340 × 96-pixel time-of-flight depth sensor in 0.18-µm CMOS. *IEEE Journal of Solid-State Circuits, 48*(2), 559-572. doi:10.1109/JSSC.2012.2227607

Niclass, C., Favi, C., Kluter, T., Monnier, F., & Charbon, E. (2009). Single-photon synchronous detection. *IEEE Journal of Solid-State Circuits, 44*(7), 1977-1989. doi:10.1109/JSSC.2009.2021920

Niclass, C., Rochas, R., Besse, P., & Charbon, E. (2005). Design and characterization of a CMOS 3-D image sensor based on single photon avalanche diodes. *IEEE Journal of Solid-State Circuits, 40*(9), 1847-1854. doi:10.1109/JSSC.2005.848173

Niclass, C., Soga, M., Matsubara, H., Ogawa, M., & Kagami, M. (2014). A 0.18-µm CMOS SoC for a 100-m-range 10-frame/s 200 × 96-pixel time-of-flight depth sensor. *IEEE Journal of Solid-State Circuits, 49*(1), 315-330. doi:10.1109/JSSC.2013.2284352

Niu, Z., Shi, J., Sun, L., Zhu, Y., Fan, J., & Zeng, G. (2018). Photon-limited face image super-resolution based on deep learning. *Optics Express, 26*(18), 22773-22782. doi:10.1364/OE.26.022773

Pancheri, L., Stoppa, D., & Dalla Betta, G. (2014). Characterization and modeling of breakdown probability in sub-micrometer CMOS SPADs. *IEEE Journal of Selected Topics in Quantum Electronics, 20*(6), 328-335. doi:10.1109/JSTQE.2014.2327791

Pancheri, L., Massari, N., & Stoppa, D. (2013). SPAD image sensor with analog counting pixel for time-resolved fluorescence detection. *IEEE Transactions on Electron Devices, 60*(10), 3442-3449.

Pancheri, L., & Stoppa, D. (2013). Sensors based on in-pixel photo-mixing devices. *TOF range-imaging cameras*. 69-89 Springer.

Payne, A., Daniel, A., Mehta, A., Thompson, B., Bamji, C. S., Snow, D., . . . Zhanping Xu. (2014). 7.6 A 512×424 CMOS 3D time-of-flight image sensor with multi-frequency photo-demodulation up to 130MHz and 2GS/s ADC. *2014 IEEE International Solid-State Circuits Conference Digest of Technical Papers (ISSCC).* 134-135. doi:10.1109/ISSCC.2014.6757370

Pellegrini, S., Rae, B., Pingault, A., Golanski, D., Jouan, S., Lapeyre, C., & Mamdy, B. (2017). Industrialised SPAD in 40 nm technology. Paper presented at the *2017 IEEE International Electron Devices Meeting (IEDM),* 16.5.-16.5.4. doi:10.1109/IEDM.2017.8268404

Peng, P., Chen, P., Kao, C., Chen, Y., & Lee, J. (2015). A 94 GHz 3D image radar engine with 4TX/4RX beamforming scan technique in 65 nm CMOS technology. *IEEE Journal of Solid-State Circuits, 50*(3), 656-668. doi:10.1109/JSSC.2014.2385758

Perenzoni, D., Gasparini, L., Massari, N., & Stoppa, D. (2014). Depth-range extension with folding technique for SPAD-based TOF LIDAR systems. Paper presented at the *Sensors, 2014 Ieee,* 622-624. doi:10.1109/ICSENS.2014.6985075

Perenzoni, M., Perenzoni, D., & Stoppa, D. (2017). A 64 x 64-pixels digital silicon photomultiplier direct TOF sensor with 100-MPhotons/s/pixel background rejection and imaging/altimeter mode with 0.14% precision up to 6 km for spacecraft navigation and landing. *IEEE Journal of Solid-State Circuits, 52*(1), 151-160. doi:10.1109/JSSC.2016.2623635

Perenzoni, M., Pancheri, L., & Stoppa, D. (2016). Compact SPAD-based pixel architectures for time-resolved image sensors. *Sensors (Basel, Switzerland), 16*(5), 745. doi:10.3390/s16050745

Portaluppi, D., Conca, E., Villa, F., & Zappa, F. (2019). Time-gated SPAD camera with reconfigurable macropixels for LIDAR applications. Paper presented at the *32nd International Congress on High-Speed Imaging and Photonics, 11051*, p. 110510J.

Privitera, S., Tudisco, S., Lanzanò, L., Musumeci, F., Pluchino, A., Scordino, A., . . . Condorelli, G. (2008). Single photon avalanche diodes: Towards the large bidimensional arrays. *Sensors, 8*(8), 4636-4655.

Ren, X., Connolly, P. W., Halimi, A., Altmann, Y., McLaughlin, S., Gyongy, I., . . . Buller, G. S. (2018). High-resolution depth profiling using a range-gated CMOS SPAD quanta image sensor. *Optics Express, 26*(5), 5541-5557.

Richardson, J. A., Webster, E. A., Grant, L. A., & Henderson, R. K. (2011). Scaleable single-photon avalanche diode structures in nanometer CMOS technology. *IEEE Transactions on Electron Devices, 58*(7), 2028-2035.

Rochas, A., Gosch, M., Serov, A., Besse, P. A., Popovic, R. S., Lasser, T., & Rigler, R. (2003). First fully integrated 2-D array of single-photon detectors in standard CMOS technology. *IEEE Photonics Technology Letters, 15*(7), 963-965. doi:10.1109/LPT.2003.813387

Schwarte, R., Xu, Z., Heinol, H., Olk, J., Klein, R., Buxbaum, B., . . . Schulte, J. (1997). New electro-optical mixing and correlating sensor: Facilities and applications of the photonic mixer device (PMD). Paper presented at the *Sensors, Sensor Systems, and Sensor Data Processing, , 3100* 245-254.

Shin, D., Xu, F., Venkatraman, D., Lussana, R., Villa, F., Zappa, F., . . . Shapiro, J. H. (2016). Photon-efficient imaging with a single-photon camera. *Nature Communications, 7*, 12046.

Spirig, T., Seitz, P., Vietze, O., & Heitger, F. (1995). The lock-in CCD-two-dimensional synchronous detection of light. *IEEE Journal of Quantum Electronics, 31*(9), 1705-1708. doi:10.1109/3.406386

Stoffel, T., Renné, D., Myers, D., Wilcox, S., Sengupta, M., George, R., & Turchi, C. (2010). No title. *Concentrating Solar Power: Best Practices Handbook for the Collection and use of Solar Resource Data (CSP),*

Stoppa, D., Mosconi, D., Pancheri, L., & Gonzo, L. (2009). Single-photon avalanche diode CMOS sensor for time-resolved fluorescence measurements. *IEEE Sensors Journal, 9*(9), 1084-1090. doi:10.1109/JSEN.2009.2025581

Stoppa, D., Borghetti, F., Richardson, J., Walker, R., Grant, L., Henderson, R. K., . . . Charbon, E. (2009). A 32x32-pixel array with in-pixel photon counting and arrival time measurement in the analog domain. Paper presented at the *2009 Proceedings of ESSCIRC,* 204-207.

Tisa, S., Guerrieri, F., & Zappa, F. (2008). Variable-load quenching circuit for single-photon avalanche diodes. *Optics Express, 16*(3), 2232-2244.

Ulku, A. C., Bruschini, C., Antolovic, I. M., Kuo, Y., Ankri, R., Weiss, S., . . . Charbon, E. (2019). A 512 × 512 SPAD image sensor with integrated gating for widefield FLIM. *IEEE Journal of Selected Topics in Quantum Electronics, 25*(1), 1-12. doi:10.1109/JSTQE.2018.2867439

Van der Jeught, S., & Dirckx, J. J. (2016). Real-time structured light profilometry: A review. *Optics and Lasers in Engineering, 87*, 18-31.

Van der Tempel, W., Grootjans, R., Van Nieuwenhove, D., & Kuijk, M. (2008). A 1k-pixel 3D CMOS sensor. Paper presented at the *Sensors, 2008 Ieee,* 1000-1003. doi:10.1109/ICSENS.2008.4716611

Veerappan, C., & Charbon, E. (2016). A low dark count p-i-n diode based SPAD in CMOS technology. *IEEE Transactions on Electron Devices, 63*(1), 65-71. doi:10.1109/TED.2015.2475355

Veerappan, C., Richardson, J., Walker, R., Li, D., Fishburn, M. W., Maruyama, Y., . . . Charbon, E. (2011). A 160×128 single-photon image sensor with on-pixel 55ps 10b time-to-digital converter. Paper presented at the *2011 IEEE International Solid-State Circuits Conference,* 312-314. doi:10.1109/ISSCC.2011.5746333

Villa, F., Lussana, R., Bronzi, D., Tisa, S., Tosi, A., Zappa, F., . . . Weyers, S. (2014). CMOS imager with 1024 SPADs and TDCs for single-photon timing and 3-D time-of-flight. *IEEE Journal of Selected Topics in Quantum Electronics, 20*(6), 364-373.

Zhang, C., Lindner, S., Antolović, I. M., Mata Pavia, J., Wolf, M., & Charbon, E. (2019). A 30-frames/s, 252 × 144 SPAD flash LiDAR with 1728 dual-clock 48.8-ps TDCs, and pixel-wise integrated histogramming. *IEEE Journal of Solid-State Circuits, 54*(4), 1137-1151. doi:10.1109/JSSC.2018.2883720

Original publications

This thesis is based on the following publications, which are referred throughout the text by their Roman numerals:

I Ruokamo, H., Rapakko, H., & Kostamovaara, J. (2017). An 80 × 25 pixel CMOS single-photon image sensor with sub-ns time gating for solid-state 3D scanning. *13th Conference on Ph.D. Research in Microelectronics and Electronics (PRIME)*, 365-368.

II Ruokamo, H., Hallman, L., Rapakko, H., & Kostamovaara, J. (2017) An 80 × 25 pixel CMOS single-photon range image sensor with a flexible on-chip time gating topology for solid state 3D scanning. *ESSCIRC 2017 - 43rd IEEE European Solid State Circuits Conference,* 59-62.

III Ruokamo, H., Hallman, L. W., & Kostamovaara, J. (2019). An 80 × 25 pixel CMOS single-photon sensor with flexible on-chip time gating of 40 subarrays for solid-state 3-D range imaging. *IEEE Journal of Solid-State Circuits, 54*(2), 501-510.

IV Ruokamo, H., Hallman, L., & Kostamovaara, J. (2019) A range-gated CMOS SPAD array for real-time 3D range imaging, *IS&T Electronic Imaging: Image Sensors and Imaging Systems Proceedings,* 357-1-357-5

Original publications are not included in the electronic version of the dissertation.

715. Ruokamo, Simo (2019) Single shared model approach for building information modelling

716. Isohookana, Matti (2019) Taistelunkestävä hajaspektritietovuo kansalliseen sotilasilmailuun

717. Joseph, Nina (2019) $CuMoO_4$: a microwave dielectric and thermochromic ceramic with ultra-low fabrication temperature

718. Kühnlenz, Florian (2019) Analyzing flexible demand in smart grids

719. Sun, Jia (2019) Speeding up the settling of switched-capacitor amplifier blocks in analog-to-digital converters

720. Lähetkangas, Kalle (2019) Special applications and spectrum sharing with LSA

721. Kiventerä, Jenni (2019) Stabilization of sulphidic mine tailings by different treatment methods : heavy metals and sulphate immobilization

722. Fylakis, Angelos (2019) Data hiding algorithms for healthcare applications

723. Juuso, Ilkka (2019) A cellular automaton environment for the complex system of speech

724. Aho, Pekka (2019) Automated state model extraction, testing and change detection through graphical user interface

725. Bergna, Davide (2019) Activated carbon from renewable resources : carbonization, activation and use

726. Nuottila, Jouko (2019) Flexibility in agile projects : Contracting practices and organisational arrangements

727. Adesanya, Elijah D. (2019) A cementitious binder from high-alumina slag generated in the steelmaking process

728. Hannila, Hannu (2019) Towards data-driven decision-making in product portfolio management : From company-level to product-level analysis

729. Saastamoinen, Ari (2020) Processing and microstructure of direct-quenched and tempered ultra-high strength steels

730. Ashraf, Muhammad Ikram (2019) Radio resource management in device-to-device and vehicle-to-vehicle communication in 5G networks and beyond

731. Elbamby, Mohammed S. (2019) Flexible duplexing and resource optimization in small cell networks

Book orders:
Virtual book store
http://verkkokauppa.juvenesprint.fi

UNIVERSITY OF OULU P.O. Box 8000 FI-90014 UNIVERSITY OF OULU FINLAND

ACTA UNIVERSITATIS OULUENSIS

UNIVERSITY of OULU
OULUN YLIOPISTO

ISBN 978-952-62-2474-9 (Paperback)
ISBN 978-952-62-2475-6 (PDF)
ISSN 0355-3213 (Print)
ISSN 1796-2226 (Online)